Design of an Electronic Speed Controller

Sub-Group: Converter

Emeric de Galembert - 5332044
Maxence Simonart - 5287553

26/06/2023

DELFT UNIVERSITY OF TECHNOLOGY

FACULTY OF ELECTRICAL ENGINEERING, MATHEMATICS AND COMPUTER SCIENCE

ELECTRICAL ENGINEERING PROGRAMME

Abstract

In this thesis, a custom 120A, 50V power converter board for a brush-less drone motor is designed as part of the Bachelor Graduation Project. The control and embedded systems parts of the project are handled by other subgroups. The power converter consists of three main parts: the inverter, the sensors and the low voltage DC to DC converters. These were implemented respectively with a triple half bridge controlled by high-/low-side gate drivers, analog current en voltage sensors, a digital temperature sensor, buck converters and an LDO. This thesis describes the design choices made for these parts and the development of a PCB temperature model. Two prototypes have been assembled and tested, showing the power converter works as intended. High voltage and current tests are still to be performed to ensure perfect operation. The temperature model yields figures that are high but realistic and the required active cooling has not been quantified. As a final note, the fully integrated ESC was able to make the motor spin at low speeds.

Preface

Group L has been asked by Fusion Engineering to build a custom, reliable ESC capable of communicating with a specific protocol. This task serves as bachelor graduation project for the students of group L. To complete the task the subgroup has to set some deadlines along the project. The first step being to design and assemble a prototype PCB, then use the test results to design and assemble a second version; in the hope to make the motor spin by the end of the project, by combining the work of all subgroups.

We would like to express our most sincere gratefulness to Jianning Dong for supervising the progress of the project, for his constant availability and responsive feedback. We would also like to thank Fusion Engineering for the support and funding, the heads of the Tellegen hall for the access to the necessary equipment and location, Ron van Puffelen and Jundong Wang for their valuable feedback on the PCB design, Quinten Luyten, our kind team mate, for always offering his help, and last but not least, Ioan Lager as the organizer of the Bachelor graduation project for all his efforts and responsiveness.

Contents

Glossary of terms

ESC	Electronic speed controller
PCB	Printed circuit board
eRPM	Electrical rotations per minute = $60 * f_{electrical}$
MOSFET	Metal-oxide-semiconductor field-effect transistor
FET	Field-effect transistor
PMSM	Permanent magnet synchronous motor
V_{BAT}	Voltage of the battery
THD	Total harmonic distortion
IGBT	Insulated-gate bipolar transistor
BJT	Bipolar junction transistor
GaN	Gallium Nitrite
SiC	Silicon Carbide
Si	Silicon
MCU	Microcontroller unit
PWM	Pulse-width modulation
EMF	Electromotive force
IC	Integrated circuit
LDO	Low-dropout regulator
HV	High voltage
LV	Low voltage
SMD	Surface-mount device

Chapter 1

Introduction

The bachelor graduation project in the Electrical Engineering bachelor at TU Delft is a 10 week long period where teams of 6 students must work in subgroups of 2 on a project. The projects must be an innovation in the Electrical Engineering field and are usually proposed by faculty professors. There is however also a possibility to bring in a project from outside the university in relation with a separate company. This is what was done for this group's graduation project. The project is coming from Fusion Engineering, a drone building start up that needed a specific custom electronic speed controller to be designed. This device receives from the drone's flight controller how fast a motor is supposed to spin and outputs power in precise sequences to the attached motor.

1.1 Problem definition

Group L has been given the task by the company Fusion Engineering to design a reliable, high power ESC with the DSHOT600 communication protocol for their bachelor graduation project. ESCs of such high power for drones are not widely available and even fewer or none are available that support this protocol *and* that are consistently reliable. This thesis covers the work of the converter subgroup. This group's task was to design a reliable inverter as well as perform different measurements useful for the control algorithm of the controller subgroup and provide the power to the controller circuit board of the communication subgroup.

1.2 Thesis synopsis

This thesis first elaborates on the environment and then sets the requirements to be satisfied by the ESC and the converter module more specifically in Chapter 2, followed by a chapter (see 3) on circuit and PCB design, with detailed explanations on topology and component choices. A chapter also discusses the attempt made to model the thermal behaviour of the system 4. After that, a chapter on testing methods and results ensues, also evaluating the performance of the system, in Chapter 5, and lastly a discussion and conclusion of the project can be found in the chapters 6 and 7 respectively.

1.3 State-of-the-art analysis

ESCs, being a very common piece of electronics, have a wide variety of topologies and designs. As for this subgroup the focus lays on the power converter hardware, a more precise look can be taken at inverters, which are even more common than ESCs. A lot of options are available for the inverters. Depending on the usage, different multi-leveled inverters can be implemented. However, more than two-level inverters are typically used for higher voltage applications. What is thus most commonly used for three phase low voltage inverters are simple triple half bridges. Aside of the inverter topology, a plethora of choices can be made at the component scale. The difficulty of this project lies in the precise component calculations, the high current and the reliability requirements, together with a very portable and light design preference. Fewer ESCs are available for comparison when setting the same requirements in addition to the specific communication protocol.
Many solutions exist on the market for sensing the different variables, from ICs to bulky external sensors. It is also possible to build sensors from the ground up based on individual components.
Concerning the low voltage power sources, again a variety of options are available, from simple resistive dividers to fully integrated buck converters. But for these too it is possible to create those from scratch to more precisely

fit the requirements and avoid over-kill.

Chapter 2

Design Requirements

Fusion Engineering tasked the team with designing an ESC that can supply 120 amps from a 12s Li-Po battery. It should communicate with the flight controller using the bi-directional DSHOT600 protocol, and be compatible wit the motors they use. Fusion Engineering prioritizes reliability over everything else, since ESC failures can cause an aircraft to fall out of the air. Industry standard efficiency of 95% is nice to have, but not a priority. The ESC must function with the "T motor mn501-s 240kv" PMSM motor.

2.1 Mandatory Requirements

Electrical requirements

- Converter must be able to handle a MOSFET switching speed of 100 kHz.
- Safely provide continuous 120A for a motor.
- Draw this current from a 12S Li-Po battery, with voltage ranging from 36V to 50.4V.
- Must drive a 3-phase brush-less motor.
- Converter must be equipped with built-in gate drivers to control the transistors.

Reliability requirements

- Temperature accross the board surface should not exceed 100°C in the vicinity of the buck converters and the DC link capacitor bank.

Interoperability requirements

- The converter must supply a 3.3V logic line to the controller with capacity of at least 100mA.
- The converter must supply a low noise 3.3V analog line to the controller with capacity of at least 100mA.
- The inverter can be controlled by six PWM signals.
- Successfully sense current in DC bus and transmit it in analog form at an update rate of at least 100kHz.
- Successfully sense current in the three phases and transmit it in analog form at an update rate of at least 100kHz.
- Successfully sense voltage across three phases and transmit it in analog form at an update rate of at least 100kHz.
- Successfully sense temperature across board and transmit it in digital form at an update rate of at least 10Hz.

Financial and organizational requirements

- The total cost of the project (parts and shipping) must not exceed €500.

Planning requirements

- The thesis must be completed by the 16th of June.
- Each subsystem must be fully working by the 30th of June.

2.2 Trade-off Requirements

- The ESC must be able to operate inside the body of the drone supplied by fusion engineering without the temperature of any components exceeding their operating temperature range.
- The efficiency of the ESC and motor should be at least 70%.
- The complete ESC must be fully operational by the 30th of June.
- Achieve a MOSFET switching speed of 1 MHz.
- The bill of material of the inverter hardware prototype should be below €70.
- Reach typical inverter industry standard efficiency of 95%.

Chapter 3

Circuit & PCB design

The motor for which the ESC is being built is a three phase PMSM (see F), 120A brush-less motor. The supply is the drone battery, a 12S Li-Po cell, with voltage ranging from 36V to 50.4V. To ensure the correct operation, of the system it was really important to make smart component choices. Comparing different devices and different ways to implement them made it possible to fulfill the efficiency and reliability requirements of the converter. Usually considered parameters were the voltage and current ratings, operating temperatures, resistances, capacitances, bandwidths and cost. The final schematic can be viewed in Figure D.1, the final PCB layout in Section E.

3.1 Inverter topology and operation

A high current, low voltage three phase inverter is required. In order to compare different inverter topologies and because three phase inverters are most often three single phase inverters next to one another, a trade-off table was constructed showing the advantages and drawbacks of different suitable single phase inverter topologies.

Table 3.1: Trade-off table of single phase inverter topologies.

Type	**Cost**	**Efficiency**	**Quantity of output voltages**
Modified half bridge	$++$	o	$-$
Full bridge	$+$	o	o
T-type	$+$	$+$	$-$
Multi level	$-$	$++$	$+$

A modified half bridge, as depicted in Figure 3.1, can generate half the voltage range over its load compared to the full bridge from Figure 3.2. This makes the half bridge less desirable because it means the motor would spin slower than with a full bridge. Indeed, the possible output voltage of this half bridge are $V_{BAT}/2$ and $-V_{BAT}/2$, while the full bridge can apply V_{BAT} and $-V_{BAT}$ over the load.

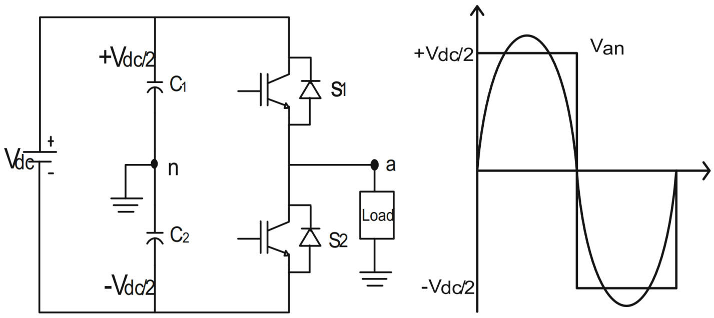

Figure 3.1: Modified half bridge inverter with a possible output waveform. (from [1]), this is not a normal half bridge as it has the ability to generate negative voltages thanks to its neutral point.

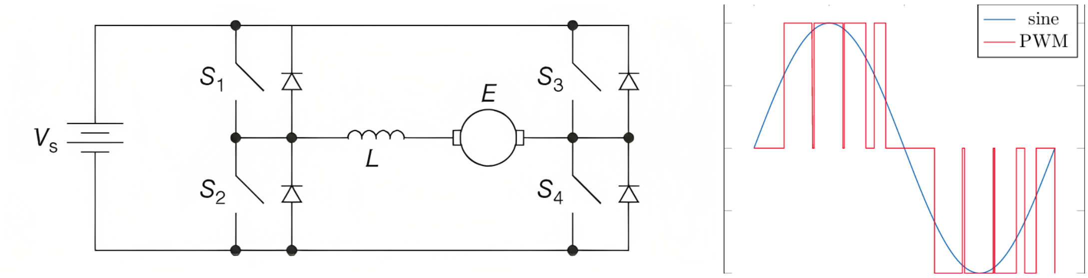

Figure 3.2: Full bridge single phase inverter (From [2]) and its generated sine wave (from [3]). Without the blue trace, it is difficult to notice a sine wave is actually trying to be generated.

The T-type inverter can achieve a lower THD than the full bridge as its switching frequency can be lower to produce the same voltage outputs.

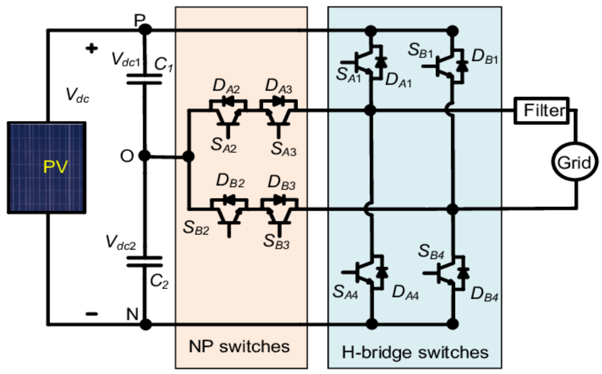

Figure 3.3: Illustration of a grid-tied five level T-type inverter from [4]. In addition to the full bridge, transistors are present to connect the load to a neutral point, giving the possibility to reach an additional voltage level.

A multi level inverter on the other hand, which is typically used when dealing with voltages larger than the transistor breakdown voltages, can generate n different voltage levels. This topology can however also be useful to lower the THD, as with the same switching frequency, the obtained equivalent number of pulses is higher than with the full bridge.

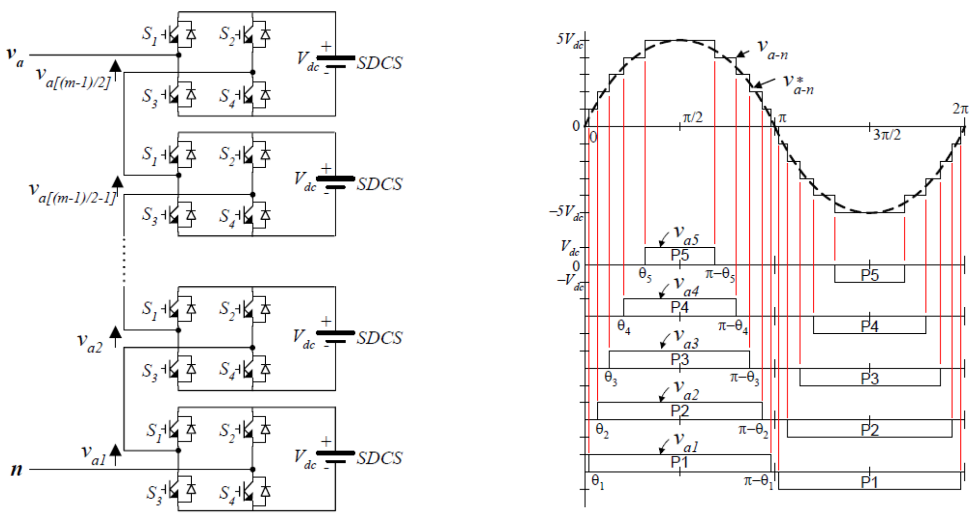

Figure 3.4: 11 level inverter and its generated sine wave. The close approximation of a perfect sine wave is important and typical of high level inverters. From [5]

The closer the sine wave approximation, the more efficient the driving of the motor. This is directly in correlation to the THD generated by the inverter.

Even though a multi level or a t-type inverter could be more efficient, these are overkill for this application, where efficiency is not one of the requirements, while cost and reliability and therefore simplicity are important requirements. The most simple single phase inverter with the highest output voltage range is the full bridge and therefore it is also the preferred choice.
Creating a three phase inverter from a single phase full bridge only requires adding one half bridge, resulting in the circuit below from [6].

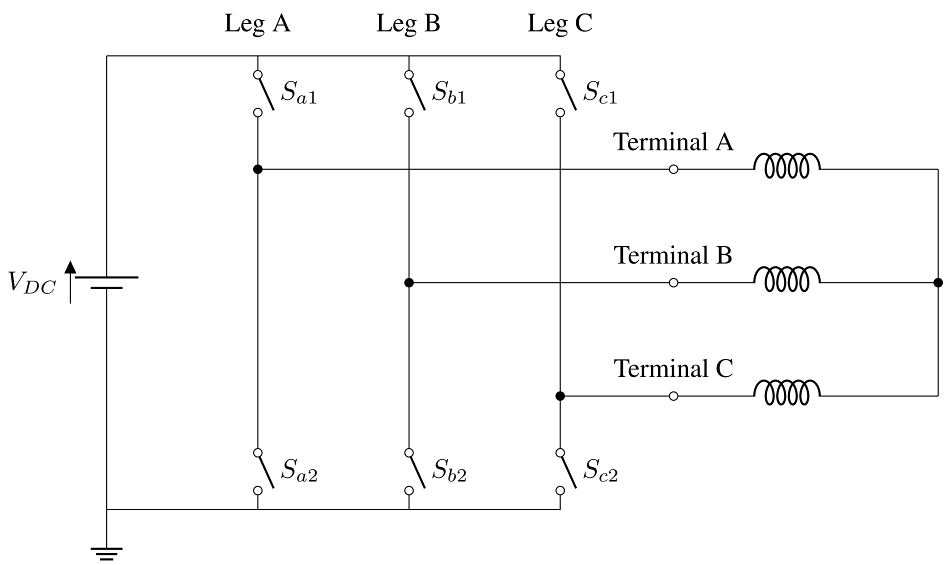

Figure 3.5: The three-phase inverter connected to the motor terminals A, B and C. The motor windings are represented as coils.

Possible Implementations

In the typical schematic of a 3-phase half bridge inverter, each phase utilizes only two switches, resulting in a total of six switches for the complete circuit. This approach offers advantages such as a smaller circuit size and a relatively straightforward switching sequence. Alternatively, it is also possible to parallel two or more half bridge assemblies per phase and synchronize their switching sequences. This configuration divides the current between the transistors, potentially reducing losses when appropriate component selection is made. Furthermore, this approach can lower the costs associated with the PCB by allowing individual traces to be smaller, compared to traces rated for 120A that would require a more advanced and expensive PCB consisting of at least six layers or external bus bars. The topic of resistance in the traces and transistors is further developed in Section 3.7.

3.2 Transistor choice

For the converter, in order to form the three half bridges from 3.1, transistors are required. To make an educated choice on the type of transistors, the most common ones were compared on different characteristics in table 3.2.

Table 3.2: Trade-off table of different transistor types. (From [7], [8], [9], [10], [11], [12], [13])

Type	**Cost**	**Voltage range**	**Current range**	**Switching speed**	**Driver circuit**	**Temperature variance**
Si MOSFET	Average	< 500V	< 250A	Very High	Easy	High
SiC MOSFET	Highest	< 1700V	< 600A	Very high	Ok	Low
GaN transistor	Higher	< 1500V	< 100A	Ultra high	Ok	Low
IGBT	High	> 1000V	< 2000A	High	Easy	Low
BJT	Lowest	< 400V	< 100A	Low	Complicated	High

The decision was made to use enhancement mode FETs for this and not IGBTs due to the higher switching speeds and lower cost of the former. Furthermore, the SiC technology, designed for significantly higher voltage applications and associated with a higher cost, was considered unsuitable for the intended system. In addition, the even higher switching speed, and more limited current of GaN transistors made this technology non suitable either. Finally, after exploring various options for the technology, Si MOSFETs were opted for, as they satisfied the voltage and current conditions at a lower price.

Due to the requirements stated in Chapter 2 there are some limitations for the MOSFETs. Being directly connected to the supply line, and because voltage spikes can occur due to motor inductance, FETs with breakdown voltages of around 60V must be selected, and with current capability of at least 120A. From the requirements, they must be able to reach a switching frequency of 100kHz as well. These three elements already limited the possibilities a lot. As a result of the high current and the high switching speed, the system can rise to high temperatures, so it was necessary to select MOSFETs with a wide operating temperature range and low losses to avoid additional heat generation. For ratings like the drain current of the MOSFET, temperature had to be taken into account as the rated maximal current decreases as temperature rises.
Different MOSFETs from the site Mouser.nl ([14]) were compared on the following specifications:

- V_{DS} [V]: Drain-Source Voltage || 60V
- I_D [A]: Continuous Drain Current at 150°C || >=120A
- T_J [°C]: Operating Junction Temperature || 150°C-175°C
- $R_{DS_{(on)}}$ [Ω]: Drain-Source on-state Resistance || minimize
- Q_g [C]: Total Gate Charge || minimize
- t_{sw} [s]: Switching Time || min(<10µs)

Multiple models were found (see Table 3.3) that meet the system conditions, but for the prototype only one was implemented, namely the one from Vishay (for data sheet see [15]) This choice was made because the gate charge was the smallest, indicating a quicker switching switching time and thus less switching losses. Another benefit of the Vishay is the low price. In addition, the Vishay data sheet offers details on the high temperature current capabilities, which is not the case for it's closest competitor, the Toshiba TPH1R306PL, meaning the current conduction capabilities cannot be guaranteed.

Table 3.3: Trade-off table of different potential Si MOSFETs.

Type	Price per unit	Break-down Voltage	Drain current at 25°C	On resistance	Gate charge	Mount type
Vishay SQJA16EP	€1.49	60V	278A	3mΩ	56nC	SMD
Toshiba TPH1R306PL	€1.96	60V	260A	1.34mΩ	91nC	SMD
Toshiba TPW1R306PL	€2.94	60V	260A	1.29mΩ	91nC	SMD
Infineon IRFS7534TRL7PP	€3.13	60V	240A	1.6mΩ	200nC	SMD

3.3 Gate Driver

To create the switching sequence gate drivers have to be added to supply a voltage to the gates of the transistors, turning them on or off. This is because the MCU is unable to supply a high enough current and voltage to the gate of the MOSFET. The speed at which the driver can switch the transistor depends on the current it can output, the propagation time and it's own internal transistor rise times. Depending on the driver the last two factors can take up to several hundreds of nanoseconds. Therefore, it was decided to opt for the 2EDS8265HXUMA3 [16] for its high output current and very low switching time compared to the other candidates from 3.4. In addition, this is a high side low side gate driver, controlling one complete half bridge at a time. Price was taken into account as well.

Table 3.4: Trade-off table of different potential gate drivers

Type	Price per unit	Rise time	Fall time	source current	sink current	Mount type
2EDS8265HXUMA3	€4.12	6.5ns	4.5ns	4A	8A	SMD
IR2125SPBF	€4.83	60ns	35ns	1A	2A	SMD
IGI60F5050A1LAUM	€9.03	6ns	5ns	1A	2A	SMD

3.3.1 Bootstrap Circuit

In order to turn on a transistor, the gate voltage must be higher than the source voltage, typically about 10 V to 20 V higher. However as the maximal potential available for the circuit is the battery's voltage, a technique must be found to boost the gate to a higher voltage. An expensive and complicated boost converter could for instance be used for this, but better solutions exist.
This is where the bootstrap circuit comes in. Bootstrapping is very common in such applications. The higher voltage for the upper MOSFET of the half bridge is obtained via a diode and capacitor system.

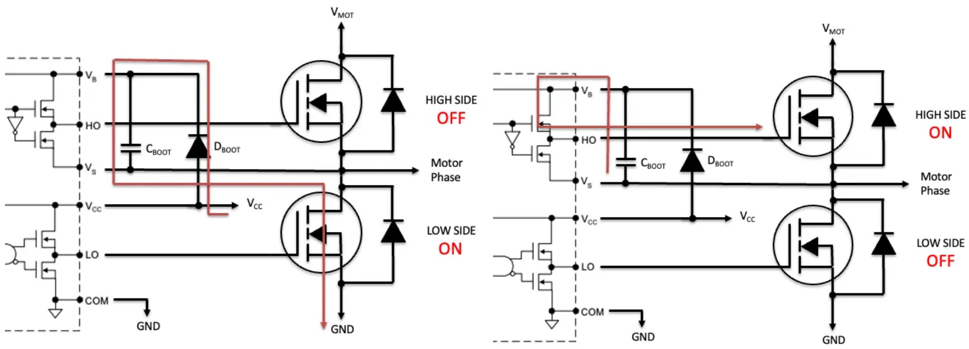

Figure 3.6: Images depicting how a bootstrap circuit works and how the current flows during charging on the left and during discharging on the right. From [17]

Initially, the capacitor is discharged with no voltage across its terminals. Pulling the phase voltage lower than V_{CC} through the activation of lower half bridge transistor, the diode will be forward biased and current will flow into the capacitor. This will charge the capacitor up, creating a voltage across it. After this, V_B will stay at a voltage of approximately V_{CC} higher than the phase, no matter the phase voltage, as the diode will be in reverse-bias mode and will prevent current from flowing back. At any time the upper MOSFET can now be turned on, by letting charge flow from the capacitor to the gate of the transistor.
Sizing and selecting the components of the bootstrap circuit is very important to ensure reliable operation. How to do this is explained in the following subsections.

Bootstrap diode

The following characteristics must be taken into account for the diode choice:

- I_{avg}
- I_{peak}
- Maximal reverse voltage
- Forward Voltage
- Reverse recovery time

The diode's average current is determined using the MOSFET's gate charge and switching frequency, because that shows how much charge per second is necessary to switch it on as desired. The gate to source leakage current can be neglected because it is orders of magnitude lower.

$$I_{avg} = Q_{gate} \cdot f_{SW} = 70\text{nC} \cdot 100\text{kHz} = 7\text{mA} \tag{3.1}$$

The peak current through the diode can be determined by looking at the duty cycle of the PWM that comes from the MCU to control the transistors. It was decided that the lowest duty cycle would be 1%, and thus the capacitor must be able to be charged in no more than 1% of the switching period. This means the peak current would be 100 times the average current and thus be 0.7A.
Additionally, the maximal reverse voltage must be at least 50.4V, but it must also be able to withstand the voltage spikes on the phase due to the motor winding inductance. The maximal reverse voltage of the diode is thus chosen to be 60V.
Taking a higher reverse voltage unfortunately increases the forward voltage, which should be minimized to have the highest possible voltage over the capacitor. This also means Shottky diodes are preferable for this application. The last point is the reverse recovery time t_{rr} that must be low according to [18], in order for the system to stay efficient and not lose too much charge from the bootstrap capacitor. These considerations led to the choice of the RB160MM-60 diode [19].

Bootstrap Capacitor

For the bootstrap capacitors the important factors are listed here:

- Capacitance formula from International Rectifiers [20]
- Maximal voltage ripple
- Maximal DC voltage

The formula to determine the size of the bootstrap capacitor according to International Rectifiers is the following one. Precise meaning of the variables can be found in their application note [20]. Briefly explained, this formula calculates the maximal voltage that can be present over the bootstrap diode and capacitor in the denominator as well as the charge necessary to turn on and maintain the FET in the on-state in the numerator. This yields a minimal required capacitance.

$$C_{Boot} \geq \frac{2[2Q_{Gate} + \frac{I_{Qbsmax}}{f_{sw}} + Q_{is}]}{V_{CC} - V_{fwd} - V_{LS} - V_{Min}} = 263\text{nF} \tag{3.2}$$

But this formula does not say what the maximal voltage ripple will be with such a capacitance. This ripple can be determined with the next formula.

$$C = \frac{Q}{V} \; so \; \Delta V = \frac{\Delta Q}{C} = \frac{Q_{Gate}}{C_{Boot}} = 0.27V \tag{3.3}$$

This equals a 2.5% ripple on the voltage of the capacitor during operation.
The maximal DC voltage over the capacitor has been chosen to be 25V, which is more than enough considering the voltage should, in theory, never reach more than 12V.
As a safety margin and to account for unconsidered inaccuracies, a bootstrap capacitor of 2.2µF was selected.

Bootstrap resistor

A resistor must be placed between the diode and the capacitor to limit the current going through the diode, preventing damage. Its value can be determined based on the peak current that can be handled by the diode. In this case it is 30A, meaning, according to Ohm's law, that the resistance must be at least equal to $\frac{11\text{V}}{30\text{A}} = 0.37\Omega$. The power dissipation capability of the resistor must not be too low, but considering this high current will flow through it for only a few nanoseconds, anything over a mW should be fine.
The selected resistance is 0.39Ω.

Gate resistor

When feeding the transistor gate with current straight from the gate driver, ringing can occur. This phenomenon is depicted in Figure 3.7.
According to an application note from Fairchild Semiconductors [22], this ringing effect can be prevented by adding a resistor. The higher the value of the resistor, the smaller the ringing at the gate, but the higher the losses and the longer the switching time.

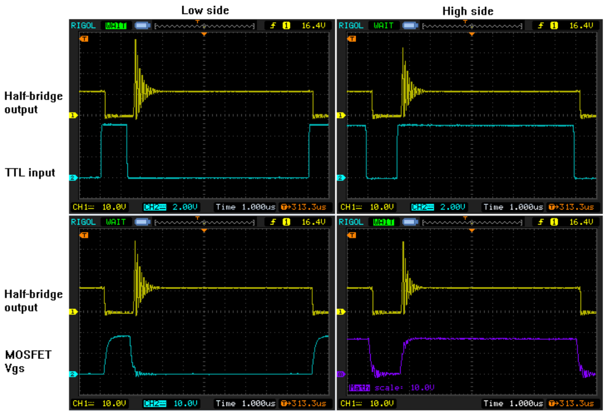

Figure 3.7: The ringing phenomenon depicted. This can cause the gate of the transistor to be turned on and off multiple times before settling on a final state. While doing this, the resistance from drain to source in the MOSFET is high and this causes many losses as well as unintentional delays. From [21]

In addition, if no resistor is placed between the gate driver and the FET, there is essentially a short circuit every time the transistor must change its on/off state. This high current can be damaging to the components and is therefore best limited by means of a resistor.
This is why a resistance of 4.7Ω is used, like recommended in the application bulletin, as this results in a peak current of only 2.34A, well under the limit of 4A of the gate driver.
As a side note, on the PCB itself these gate resistors are one of the only through-hole components, this has been done on purpose to facilitate half bridge tests by being able to control the gates of the FETs without the gate drivers, as connectors can easily be attached to the resistor legs.

Decoupling capacitors

Around the gate driver, two additional decoupling capacitors must be added. One at the 3.3V input for stabilization of the logic supply line, which does not require a large size (100nF suffices) knowing it only consumes a couple mA. And one at the V_{CC} input.
The size of the latter must be calculated appropriately. Texas Instruments published an application report [23], arguing the decoupling capacitor for the V_{CC} line should be ten times the size of the bootstrap capacitor. This should indeed be plenty enough and results in a capacitor of 22µF with a voltage rating of 25VDC

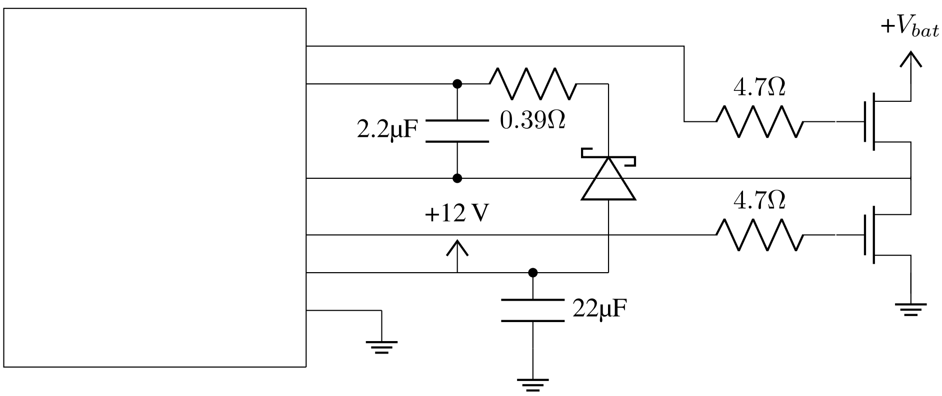

Figure 3.8: This circuit depicts the components of the team's complete bootstrap circuit as well as the components of the half bridge.

3.4 Sensors

Controlling an ESC requires sensors, some to guarantee safe operation like the temperature sensor, some for precise motor control like the current and voltage sensors. Monitoring temperature on the ESC is most crucial in

the middle of the three half bridges as they are the ones heating up the most, for this, a digital temperature sensor with a wide operating range and good accuracy was preferred over analog sensors which tend to be less accurate.
In order to monitor the phase voltages and the back EMF while the motor is spinning, one voltage divider was added to every phase, serving as voltage sensor. This voltage divider brings down the voltage from 59V to 3V, with resistors of $56\text{k}\Omega$ and $3\text{k}\Omega$. The losses caused by these resistors lie in the mW range and can thus be considered as negligible. In parallel to the smaller resistance, a tiny capacitor can be added in order to measure a continuous voltage without it being influenced by the PWM signal fed into the transistors of other half bridges.

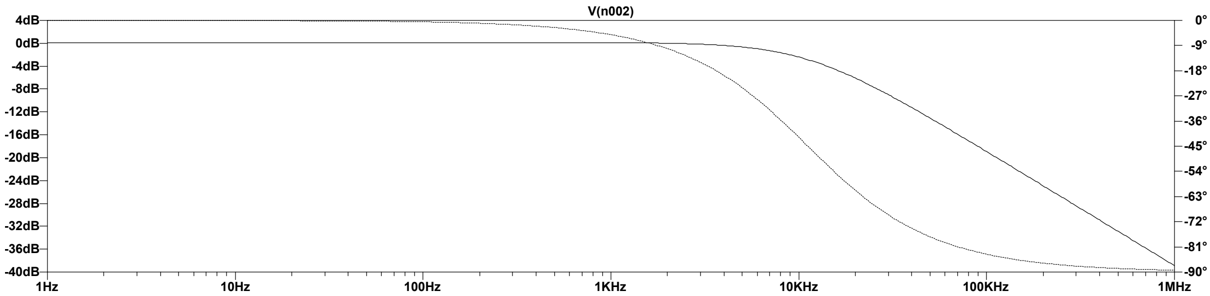

Figure 3.9: Bode plot of the transfer function of the resistor and capacitor of the phase voltage sensor circuit, showing a 19dB attenuation at 100kHz and an 85° phase shift, for a 5nF capacitor.

The value for the capacitor can be chosen as follows: it's goal is to filter out the influence of the transistor switches of which the frequency is 100kHz. This means that the cut off frequency of this RC system must be smaller than 100kHz. For this, a capacitance of 5nF suffices. This capacitor however can cause a significant phase shift in the measurements. It is for this reason that these filtering capacitors have not been added on the inverter PCB, but rather on the controller PCB, where the control subgroup can choose by themselves what level of filtering and phase shift they would like to achieve.

Table 3.5: Trade-off table of different potential analog current sensors, all with sufficient current measurement range of up to 160A at least.

Type	**Price per unit**	**Implementation**	**Sensitivity**	**Efficient**	**Measure AC**	**Bandwidth**
Shunt with amplifier	€5	Complicated	18mV/A	<15W loss	No	500kHz
Current transformer	€8+	Impractical	Arbitrary	<1W	No	5kHz
Hall effect with core	€10	Ok	10mV/A	<1W	Yes	120kHz
Core-less Hall effect	€4.5	Ok	<8mV/A	<1W	Yes	240kHz

Finally, current sensors are widely available in many different formats such as a shunts, ICs or different formats of Hall effect sensors. Table 3.5 shows the advantages and drawbacks of each type of sensor.
The main issue with the shunt is the more complicated implementation, as an additional amplifier is needed and all the current must pass through it, making traces larger and less efficient. In addition, making it possible to measure currents in both directions increases the amplifier's complexity.
Implementing a coil around the conductor, only works for AC and is difficult to implement on a PCB too.
The last considered options are Hall effect sensors. The one with a core must have all the current pass through it like the shunt which makes it less efficient due to the additional connection losses. The core-less version, however, has no physical connection to the trace, but merely senses the magnetic field caused by the trace in its vicinity. These core-less sensors, unfortunately, need to be calibrated to their real-world sensitivity, once mounted on the PCB. The latter, more precisely the "ACS37612 Standalone Coreless Differential Current Sensor IC" from Allegro, was selected for measuring currents in the ESC based on the trade-off table.
It is useful to determine the expected sensitivity in mV/A of the sensor, firstly its sensitivity of 10mV/G can be found in the data sheet ([24]). The distance between the middle of the trace and the sensors in the IC is approximately 2.5mm. Using the magnetic field formula, the field in function of the current is found:

$$B = \frac{\mu_0 \cdot I}{2 \cdot \pi \cdot r} \tag{3.4}$$

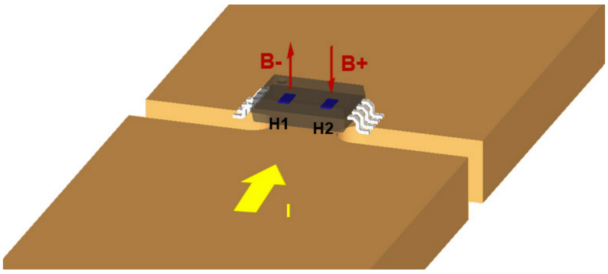

Figure 3.10: This figure (from [24]) depicts the operation of the chosen Hall effect sensor. In the final prototype, due to the traces that are on top of the PCB, this sensor has been placed on the bottom of the PCB to sense the current from underneath.

$$\frac{B}{I} = \frac{\mu_0}{2 \cdot \pi \cdot r} = 8 \cdot 10^{-5} T/A = 0.8\text{G/A} \tag{3.5}$$

Finally this can be converted to the desired variable of mV/A with the sensor sensitivity:

$$\frac{U}{I} = 0.8\text{G/A} \cdot 10\text{mV/G} = 8\text{mV/A} \tag{3.6}$$

This means the sensor can measure currents of up to 206A in theory. However, as the formula for the magnetic field is only an approximation of the field on this PCB, the sensitivity is expected to be lower.
Just like the gate drivers, the current and temperature sensor need a 100nF decoupling capacitor at their 3.3V input for additional stability of the analog output.

3.5 DC link capacitors

In addition to small decoupling capacitors for IC's, somewhat larger decoupling capacitors are needed for the high voltage and high current parts of the circuit. These are necessary to provide high currents to the transistors while reducing noise for the rest of the systems, caused by the high transistor switching speed. In addition, they counterbalance the inductance of the cables to the battery of the drone. The size of the capacitors can be determined based on the allowable voltage ripple on the line. The team has decided the ripple could reach at most 5%, so about 2.5V, in order to guarantee high performance of the ESC. When the capacitor bank alone is providing all of the current for 10 switching cycles or about 0.1ms, this means the delivered charge must be 120A $\cdot$ 0.1ms = 12mC. When the capacitors lose this much charge, their voltage is not allowed to decrease by more than 2.5V, meaning their capacitance should be at least $C = \frac{Q}{\Delta U} = 4.8\text{mF}$.
When following formulas from [25] that more realistically assume the battery provides all the DC current and the capacitors provide all the AC current consumed by the switches, the DC link capacitance can also be estimated:

$$C \geq \frac{i_C}{\Delta V \cdot f_{sw}} \tag{3.7}$$

$$I_C = I_{N,rms} \cdot \sqrt{2M \left[\frac{\sqrt{3}}{4\pi} + cos^2\phi \cdot \left(\frac{\sqrt{3}}{\pi} - \frac{9}{16} M \right) \right]} \tag{3.8}$$

Where $I_{N,rms}$ is the inverter phase rms output current. Maximizing I_C to account for the worst case yields the following equation.

$$I_{C,max} = I_{N,rms} \cdot \sqrt{2 \cdot 0.5 \left[\frac{\sqrt{3}}{4\pi} + 1^2 \cdot \left(\frac{\sqrt{3}}{\pi} - \frac{9}{16} \cdot 0.5 \right) \right]} = 78\text{A} \tag{3.9}$$

Filling $I_{C,max}$ back into eq. 3.7 together with a 2% ripple of 1V yields a capacitance of 780µF, which is a more reasonable value.
Increasing the capacitance a little to provide enough current at startup, where the battery current may be limited, is reasonable, therefore, a capacitor bank with a maximal capacitance of 5mF was designed. The team however only expects to utilize one or two of the five capacitor spots depending on the motor that is attached to the ESC.
The selected capacitors were electrolytic capacitors. As this is a simple prototype, long lifetime of the components is not yet important. The alternative to electrolytic capacitors were film capacitors; their life time may be up to three times longer [26], but these are generally more expensive, and given the short life of the prototype, not worth the extra cost.

3.6 Step down converters

From the Program of Requirements in Section 2.1, the converter PCB must supply two types of low voltages to the controller board and also needs a separate 12V supply for the gate drivers.

Digital 3.3V

Creating DC to DC buck converter circuits from scratch is cheap and fully optimized to the circuit needs. But this is also more complicated than buying all-in-one switching regulator buck converters. The team opted for the latter as the price is still reasonable and the implementation is really simple. In addition, the power to be delivered for the controller board is very little, so a very powerful converter is not necessary and a 500mA converter largely suffices. The only requirements were to add capacitors at its in- and outputs as specified in the data sheet [27]. This will be used as source for all the digital 3.3V components.

Digital 12V

The same reasoning as for the digital 3.3V supply was used for the 12V supply, even though the current requirements are slightly larger for the 12V. The current drawn from the gate drivers is on average about 30mA, while the 3.3V analog supply that is fed by the 12V source is expected to not draw more than 100mA. This means a 500mA DC to DC buck converter suffices for the 12V source too. This converter is from the same series as the 3.3V one.

Analog 3.3V

As most of the sensors are analog, in order to be converted accurately and to minimize the effect of noise on the measurements, a more stable analog 3.3V source is necessary. This source is only used by the analog to digital converters of the MCU on the controller board and by the four current sensors on the inverter board to make sure no logic switching noise is present on the line. The current sensors are expected to work with 3.3V while drawing a current of at most 40mA all-together. For attaining low noise sources there are different options, either an efficient buck converter with strong filters, or an LDO (low-dropout regulator). The latter is less efficient but simple and most often comes in the form of a simple IC. It works with internal feedback and adapts a resistor on the inside, in real time, to keep the output voltage as flat as possible, even though some noise might be present on the input. As there will be a voltage drop over the internal variable resistance, the source of an LDO must always be higher than its output, which is the reason for which the digital 12V source was used. In addition this is more efficient than stepping down straight from 50V to 3.3V using only a resistor. The selected LDO's data sheet is the following: [28].

3.7 PCB Traces

Making a PCB suitable for 60V, with low current is fine as long as the clearance between traces is high enough. However in the context of this ESC design, very high currents are expected to pass through the PCB. The solution across the industry for this is to either have a thicker copper layer, to have a trace run through multiple PCB layers or to have an external bus bar on the PCB surface. If one does not do that, the width of a 120A trace with a length of 2 inches that can rise up to 150°C is calculated using the following formulas from [29]:

$$A = \left(\frac{I}{k \cdot T_{Rise}^{b}}\right)^{\frac{1}{c}} \tag{3.10}$$

$$W = \frac{A}{t \cdot 1.378} \tag{3.11}$$

Where A is the area, W is the width, $b = 0.44$, $c = 0.725$, $k = 0.024$ for internal copper layers and $k = 0.048$ for external layers running on the PCB surface, when using 2oz/ft^2 of copper for conducting layers.
This amounts to a trace width of 56mm if it is not exposed to the outside air, and 22mm if it is. Those widths far exceed the component widths, preventing the implementation of components that are not wider than this.
The advantage of externally running traces are multiple. Firstly they can dissipate more heat when reaching higher temperatures, meaning they can be smaller while still being able to conduct the same amount of current. Secondly, solder can be melted on top of these in order to increase the conductivity. This means it is possible to have a smaller trace on the surface, while still having the possibility to conduct high currents. On the second prototype, copper wires were even added inside of the melted copper to increase the conductivity even more.

Assuming a trace temperature of 150°C and a current of 120A, the allowed resistance of the trace is 1mΩ. The maximal width of the trace is however also determined by the used components, more precisely the MOSFETs, where the pins of the source must not touch the pin of the gate. According to the MOSFET's data sheet, this means the trace can have a width of 4mm, which is much smaller than the ideal 22mm.
This is where additional solder comes in handy. With a resistivity of 17 µΩ·m for lead free solder, an easy calculation can be made to obtain the necessary tin to add on the board. The resistance of a trace of 4mm width and 5cm length (this is the length of the trace of the HV DC bus on prototype 1) is 5mΩ, which is 5 times higher than the allowed value. Therefore the resistance of the added solder must be roughly 1mΩ to make sure the desired value is reached. Using the formula $R = \rho \cdot L/A$, an area of 8.5cm^2 of solder is required. This is unfortunately also not feasible. As the effect of adding copper wires in the additional solder is not easily quantifiable, the last two remaining options are to make two (or more) traces per phase, with two (or more) transistors in parallel every time, allowing more current to pass through. Or to add active cooling on the board. The team decided, as the test motor only draws a peak current of 25A, to stick with the single traces for easier design and assembly and cool the traces with fans if necessary.
Eventually the resistance of the traces with additional solder were measured to be $\approx$ 4mΩ at room temperature, this would yield a power loss of 120^{2}A·4mΩ =58W.

3.8 PCB Layout

In Section E many renders and images of the PCB layout can be seen. For the second prototype, a 4 layer PCB was designed, resulting in a more compact ESC. In addition, it allowed the team to clearly separate digital and analog signal lines, considerably reducing the noise on the sensitive analog lines. It has also been made sure that each signal or power line almost always has it's return path to ground precisely on top or under it. This also reduces noise significantly. The initial goal was to separate the layers as follows.

1. Top: High power, digital signals and digital ground
2. Inner 1: Digital signals
3. Inner 2: Analog ground
4. Bottom: Analog signals

However, in order to reduce the routing complexity and the size of the PCB, gate drivers were placed on the bottom, therefore a digital zone is also present on the bottom layer, but it has its own digital ground return paths right above it. In the end, the layers ended up in the following way:

1. Top: High power, digital signals and digital ground
2. Inner 1: Digital signals
3. Inner 2: Analog ground and digital ground
4. Bottom: Analog signals and digital signals

Chapter 4

Temperature model

The team simulated a temperature model to better quantify the power lost in heat in the circuit. This chapter analyzes these behaviors and their equations to explain the model's results. In addition to the temperature model, the team researched heat dissipation itself more in depth, however as this is less relevant for this chapter, the heat dissipation section has been included in the Appendix under Section A.1.
Thermal behaviour of components can be represented by an equivalent electrical circuit, based on power losses and thermal resistance. The equivalent circuit that represents the situation best can be viewed in Figure 4.1.

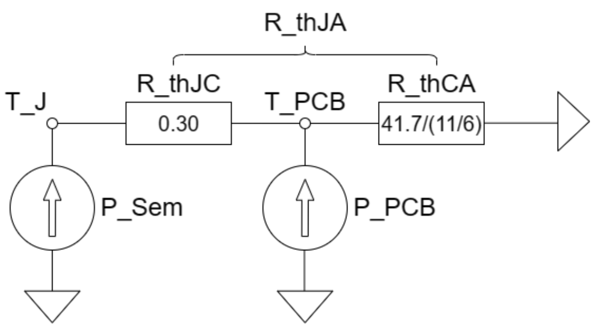

Figure 4.1: Circuit modeling the power losses and dissipation of heat in the actual system. The power lost is represented as a current source and the dissipation of heat is represented by a resistance.

In this model P_{Sem} represents the losses occurring in one transistor, P_{PCB} are the losses happening in the traces around that transistor, T_J the temperature at the junction of the MOSFET, T_{PCB} the temperature of the PCB itself, R_{thJC} the thermal resistance from the junction to the case of the semiconductor equal to 0.3°C/W [15], while R_{thJA} equals 42°C/W [15], and lastly R_{thCA} being the thermal resistance from the case to the ambient air. calculated to be,

$$R_{thCA} = \frac{R_{thJA} - R_{thJC}}{\frac{11}{6}} = \frac{42 - 0.3}{\frac{11}{6}} \tag{4.1}$$

The factor $\frac{11}{6}$ comes from the difference in setup between how the value from the datasheet [15] was obtained, and how the MOSFET was implemented for the prototype. In the case of the datasheet a PCB surface, onto which the transistor is soldered, of 1inch^2 or $\approx 6.45\text{cm}^2$ taken into account, whereas the prototype has about 12cm^2 of PCB area per FET resulting in a scaling factor of $\frac{11}{6}$.

4.1 Modelling of losses

Before being able to determine the junction and PCB temperatures, the losses in the circuit must be determined. Three types of losses were accounted for: the conduction losses in the transistor P_{MOSFET} and the traces P_{PCB}, and the switching losses P_{SW}.
Conduction losses happen everywhere in a circuit as a result of the current passing through the system. The higher the current or resistance, the higher the losses. The first type of conduction losses to be calculated take place in the MOSFETs. From Ohms law, the power dissipated in a resistor equals $I^2 \cdot R$. Because at full power, at any time

there are only two out of the six FETs that are turned on, while the formula assumes there is continuous current flowing through the transistor, the dissipated power per transistor must be scaled by 2/6.

$$P_{MOSFET} = \frac{1}{3} I_{ph}^2 R_{on} \tag{4.2}$$

With I_{ph} being the phase rms current in the motor, that can be calculated using the relation between the power in the system and the three phases (see Appendix A, equation A.8), and R_{on} the on-state resistance of the MOSFET. The on-state resistance depends on temperature as at higher temperatures, more electron collisions take place, and this was taken into account in the MATLAB code B that was written for the temperature model simulation. This resistance change was modeled using information from the transistor data sheet [15] and by making a fit of the function (see Appendix B).

The second type of conduction losses are found in the traces of the circuit. These are also calculated based on Ohms law, however the scaling factor is now 1/6, because we are modelling the temperature for one MOSFET out of the six. Because the traces are located in a relatively symmetrical manner around the transistors, it would result in biased temperatures to account for more than 1/6th of the trace losses in the temperature model for one FET and its environment.

$$P_{PCB} = \frac{1}{6} I_{ph}^2 R_{trace} \tag{4.3}$$

With the variable R_{trace} representing the resistance of the traces in the PCB. A measurement was made between both battery terminals while activating both transistors of a half bridge. The resulting value was $\approx$ 4mΩ. However, this resistance too varies with temperature. To model this, a formula was used that can be found in Appendix A at equation A.9.

Lastly, the switching losses, which solely take place during the transition periods between the on- and off-states of the FETs, are determined. These are mostly frequency dependent as a higher frequency leads to higher losses. The formula to define them is the following one [30]:

$$P_{SW} = \frac{V_{dc}(t_{on} + t_{off}) I_{av} f_{sw}}{4\pi} \tag{4.4}$$

With V_{dc} the supply voltage of at most 50.4V, t_{on} the turn on time of 17ns [15], t_{off} the turn off time of 40ns [15], I_{av} being the average current through one switch, which was obtained from the formulas A.10 in Appendix A, and f_{sw} the switching frequency equal to 100kHz.

Using the conduction and switching loss equations it is then possible to find the temperature of the junction and of the PCB. However, an iterative function must be implemented to calculate the new resistance values at the determined temperature and then after this, calculate the new losses and the new temperatures. The temperature for the first step of the iteration can be taken to be the room temperature of 25°C. The equation to obtain the junction temperature comes from Ohms law from the model in Figure 4.1 and is described as,

$$T_J = T_a + P_{Sem} \cdot (R_{thJC} + R_{thCA}) + P_{PCB} \cdot R_{thCA} \tag{4.5}$$

With T_a the ambient temperature around the PCB set at 25°C, $P_{Sem} = P_{MOSFET} + P_{SW}$, and the rest of the variables identical as explained before. For the PCB temperature the formula was also derived from Figure 4.1 and is equal to,

$$T_{PCB} = T_a + (P_{Sem} + P_{PCB}) \cdot R_{thCA} \tag{4.6}$$

With T_a again the ambient temperature and R_{thCA} identical to 4.5 as well.

Combining all those formulas in a MATLAB script, an attempt was then made to run the model and obtain results. The plotted temperatures, in Figure 4.2, represent the behaviour of the system in steady state. It was also considered to create a transient thermal behaviour model, but it was not developed due to the lack of time and also as it might not be very useful considering the ESC will power the motor for tens of minutes.

The acquired temperatures are quite high, this is clearly due to the high current even though the resistance is not so high. In addition this model assumes there is only passive cooling. In order to obtain precise temperature values, an iterative function should be implemented for the temperature, power losses and varying resistance, however this was only hard coded and is therefore less precise.
Since the reached temperatures of 870°C for the junction and 860°C for the PCB far exceed the component limits (175°C for the transistors, 85°C for other components), full power would lead to a failure of the ESC. Some form

of cooling is thus a necessary implementation, this can be done by allowing airflow or by installing heat sinks and fans. For the latter, since the MOSFETs are surface mounted, it would only be possible to install heat sinks to the PCB itself. More research and better simulation should be ran to define exactly how much cooling should be added. On the other hand, transistors and traces could be placed in parallel to reduce the losses in the first place. As the temperature must roughly be divided by $\sqrt{10}$ for correct operation, this means that without active cooling, three to four of the transistors that were selected should be placed in parallel. This is too many, but different transistors such as the Toshiba TPH1R306PL which have lower on resistances of about $1\text{m}\Omega$ greatly reduce the necessary number of parallel transistors to one or two. If active cooling is added, this could be further reduced to only one, resulting in an operational ESC, even at full power of 120A.

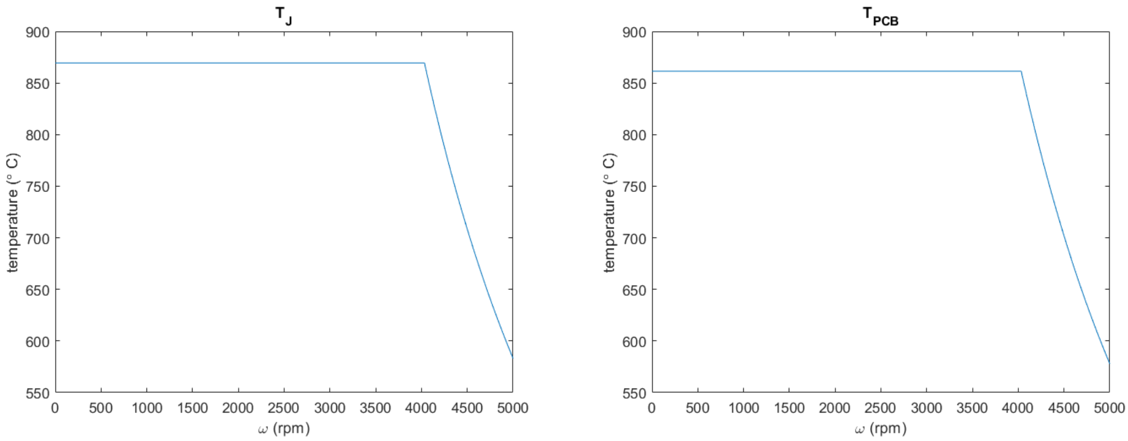

Figure 4.2: Left: Graph of the relation between the rotational speed and the junction temperature. A decrease can be seen at higher speeds due to a decrease in the current being pulled by the motor. (see equation A.8)
Right: Graph of the relation between the rotational speed and the PCB temperature. The same decrease can be seen as with the junction temperature, as the current plays an identical role in the loss formula.

Other simulations for the dissipation of heat and losses in the system have been done. In those losses are compared with the junction temperature and the rotational speed. A plot was also made of the on-resistance dependent on the junction temperature. This can be found in Appendix C.

Chapter 5

Test and performance evaluation

The first prototype did not make it past the testing phase as its gate drivers were unable to turn on the MOSFETs. The other components did work successfully on the other hand. Once the second prototype was designed and assembled the team decided to run some tests to verify the different elements and their operation. Quickly the team came to the realisation that a trace was missing around all three gate drivers, unlike on the first prototype, between the bootstrap capacitor and the phase. Once this wire was added to the circuit, it showed a normal behaviour.

Due to the lack of time and easy access to high power DC supplies, the testing of the PCB was realised with a supply of 16V hooked up to the battery terminals on the PCB. The team tested the upper FETs by using a pull down resistor of 1kΩ between the phase and the ground, while the lower FETs were tested by using a 1kΩ pull up resistor to the HV DC bus. All six of the FETs worked as intended for frequencies ranging up to 1MHz. The team did not test the capabilities north of 1MHz as this was the highest speed they hoped to achieve as a trade-off requirement. A measurement of the 10kHz and 100kHz tests are displayed in Figure 5.1.

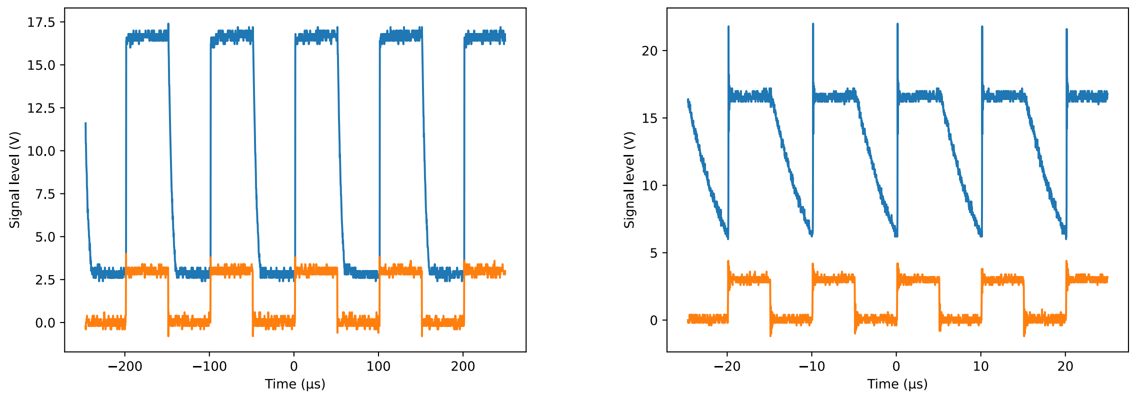

Figure 5.1: Test of the upper MOSFET of phase C at a frequency of 10kHz and 100kHz with a pull down resistor. The orange waveform coming from the function generator represents the PWM signal fed to the gate driver, while the blue waveform is the phase output. Clearly, it can be seen the pull down is not strong enough to lower the phase voltage fast enough.

Under 100Hz, the upper MOSFET may turn off before the end of the period due to the gate to source leakage current and other losses that discharge the bootstrap capacitor too much. This issue can be resolved by quickly turning it off completely and turning on the lower FET of the half bridge. This will charge up the bootstrap capacitor again, allowing the upper FET to be turned on a new time. However this limitation should not affect the operation of the ESC at all since the control algorithm plans on switching the transistors at a constant frequency of 100kHz.

The inverter was also tested by activating all six MOSFETs in a trapezoidal control sequence. No motor was attached, but resistors were installed in a WYE connection on the phases. The test output can be seen in Figure 5.2.

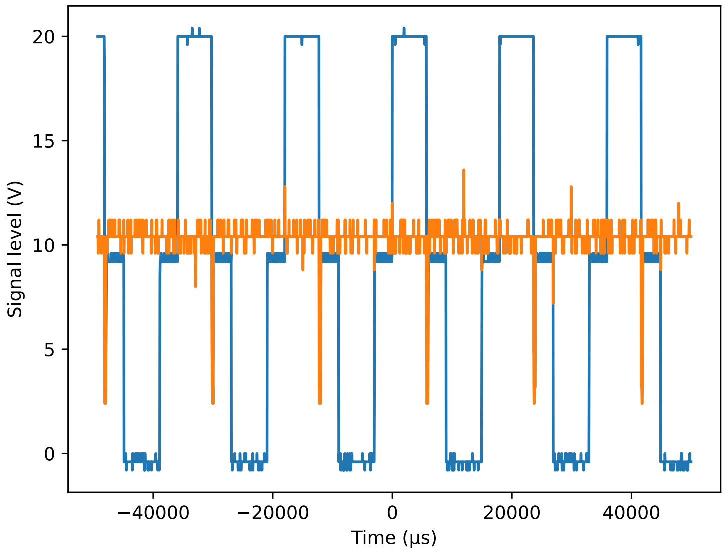

Figure 5.2: Test of all phases when fed with a trapezoidal waveform sequence generated by the controller board that was attached to the inverter board. The inverter performs as expected. The blue waveform represents the output of phase B, while the orange line is the voltage at the neutral point between the three resistors.

Finally, the motor was attached as well and the completed ESC was able to make it spin at low speeds in an open loop manner.
As for the sensors, the temperature sensors communicated digitally with SPI as expected, giving detailed estimations of the PCB temperature to the MCU.
The voltage sensors divided the voltage correctly and measurements were successfully returned analogously to the MCU.
In order to test the current sensors, currents of 2.3A (max. DC supply current) were pushed through every phase as well as the DC link. This made all four of the sensors change their voltage output by 6mV, meaning the sensitivity of the sensors is 2.6mV/A. This sensitivity is a bit lower than expected, which is unfortunate, however accurate current measurements are not necessary for the control subgroup, meaning this will not cause significant issues. Additional tests regarding noise on the analog sensor lines could still be executed, this can serve for good filtering capacitor selection on the controller board.

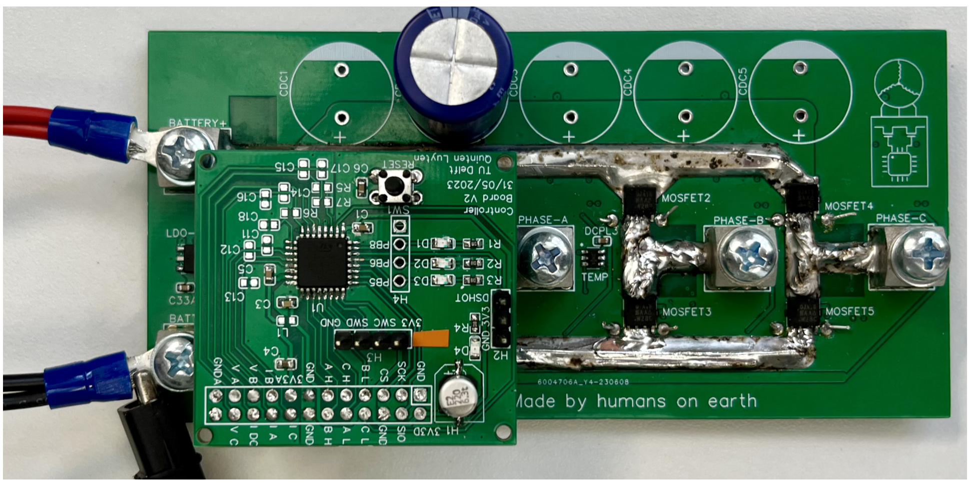

Figure 5.3: Picture of the top of the PCB after assembly, during testing. The small PCB is the the communication subgroup circuit board that simply plugs into the header of the converter PCB.

Chapter 6

Discussion & Recommendations

6.1 Discussion

Throughout the course of the project the team met quite some obstacles. As it turns out, designing a high power ESC is not *that* easy after all.
The biggest one definitely was the limited duration of the project. Due to the nature of the work, with periods where the members had to wait on the orders to arrive, deadlines were all following each other. This meant that any delay had a significant impact on the rest of the project. Next to the scarcity of time, the group also had to familiarize themselves with the topic first, as none of the members had a considerate amount of knowledge or experience in the field. Aside of the topic they also had to learn how to use software like PCB designing software or pieces of equipment. It was also the first time the members had to do SMD soldering.
Testing was another big challenge, with both prototypes not working in the beginning, a lot of effort was spent on debugging them and understanding where mistakes were made or why the circuit would not operate. More on the testing and debugging can be found in Chapter 5.
Considering the design requirements from Chapter 2, the only mandatory requirement that was not met was to safely provide 120A to a motor. This has indeed not been verified and without intensive active cooling, the PCB is not expected to be able to handle such high currents.
On the other hand, the MOSFETs were able to achieve a switching speed of 1MHz and the bill of material was under €70, as the PCB itself costed approx. €5 and the components around €60.

6.2 Future work

A few modifications could still be done on the inverter: if paying more attention to efficiency, different components might be selected to increase it. The idea of putting transistors in parallel still has to explored further. This also has an impact on the component selection and thermal behaviour of the system, a smart choice would influence the performance greatly.
Some more research should be done on the temperature model to make it more accurate. It could be explained in further details how heat dissipates through the circuit and where losses happen. Also making precise calculations, to define how much cooling is necessary and what type of cooling would be best to implement, can be useful. Besides this an iterative temperature model could be implemented in the current code to obtain more precise values for resistance, temperature and power losses.

Other than technical changes, a data sheet should be written for the ESC to document its functions, working conditions, measured data, modules and components, and any form of additional information.

Chapter 7

Conclusion

The converter module was completed in time and is able to function as intended. All the different parts fulfilled their roles. The inverter, in the form of three half-bridges with a total of six Si MOSFETs, reached a switching speed of 1MHz. These bridges were controlled by three extremely fast high side/low side gate drivers, utilizing a working bootstrap circuit to obtain a high enough gate voltage for the upper MOSFET.
The voltage sensors, implemented in the form of simple voltage dividers, give accurate readings, making it possible to reliably control the motor. The digital temperature sensor in the form of an IC also has a good resolution, assuring a safe operation of the system and avoiding unexpected failures. The current sensors, implemented as core-less and contact-less Hall effect sensors, are accurate enough to be used by the control algorithm. And the different step-down converters are capable of supplying the required voltages with low enough noise levels to the sensors and to the MCU on the controller circuit board.
Two prototypes were designed and assembled in total. The second version contained significant improvements over the first version.
The custom PCB lay-out was successful too, as the tests all confirmed the correct operation of the circuit.
Besides this, the temperature model is able to simulate the thermal behaviour of the system and plot the resulting temperature rises generated by the power losses. This model led the team to realise that parallel transistors and traces would greatly improve efficiency and reduce the need for active cooling. This also helped the team to conclude that with different transistors and a little active cooling, the inverter would be able to operate at full power sustainably.

Bibliography

[1] R. V. R. M. Pandit L. Srivastava and J. C. Bansal, *Intelligent Computing Applications for Sustainable Real-World Systems* (Proceedings in Adaptation, Learning and Optimization). Springer, 2020, vol. 13.

[2] B. Ferreira and W. van der Merwe, *The Principles of Electronic and Electromechanic Power Conversion A Systems Approach*. John Wiley & Sons, Inc., 2014.

[3] kkazem. "Introduction to power inverter design, 12/24 vdc input, 120 or 240 vac, 50/60 hz output." (2021), [Online]. Available: https://community.element14.com/technologies/power-management/b/blog/posts/power-inverter-design-100w-12-24-vdc-input-120-or-240-vac-50-60-hz-output.

[4] E. M. A. M. Aly M. Orabi and M. Shoyama, "An enhanced pwm method for loss balancing of five level t-type inverter in pv systems," in *Proceedings of the IEEE International Conference on Circuits and Systems (ICCS)*, IEEE, Fukuoka, Japan, Feb. 2019, pp. 2530–2535.

[5] D. Poornima, R. Bharath, and F. Andrew, "A single source cascaded multilevel inverter," *International Journal of Electronics Engineering & Applications*, vol. 3, p. 22, Jan. 2014. DOI: 10.30696/IJEEA.VII.II.2019.37-46.

[6] M. van Schagen and Y. Brodskaya, *Control algorithm for a high power electronic speed controller*, 2023.

[7] T. E. D.
bibinitperiod S. Corporation, *Basic knowledge of discrete semiconductor device*, https://toshiba.semicon-storage.com/content/dam/toshiba-ss-v3/master/en/semiconductor/knowledge/e-learning/discrete/discrete-basic-chap3_en.pdf, 2022.

[8] Onsemi. "Gan vs. sic transistors." (2021), [Online]. Available: https://www.powerelectronicsnews.com/the-difference-between-gan-and-sic-transistors/.

[9] A. Privat, H. Barnaby, B. Tolleson, K. Muthuseenu, and P. Adell, "Temperature dependence of bipolar junction transistor current-voltage characteristics after low dose rate irradiation," *Microelectronics Reliability*, vol. 113, p. 113 947, 2020, ISSN: 0026-2714. DOI: https://doi.org/10.1016/j.microrel.2020.113947. [Online]. Available: https://www.sciencedirect.com/science/article/pii/S0026271420307782.

[10] J. W., "A comparison between si and sic mosfets," *IOP Conference Series: Materials Science and Engineering*, vol. 729, no. 1, p. 012 005, 2020. DOI: 10.1088/1757-899X/729/1/012005. [Online]. Available: https://dx.doi.org/10.1088/1757-899X/729/1/012005.

[11] J. Wang and X. Jiang, "Review and analysis of sic mosfets' ruggedness and reliability," *IET Power Electronics*, vol. 13, no. 3, pp. 445–455, 2020. DOI: https://doi.org/10.1049/iet-pel.2019.0587. [Online]. Available: https://ietresearch.onlinelibrary.wiley.com/doi/abs/10.1049/iet-pel.2019.0587.

[12] N. Kaminski and O. Hilt, "Sic and gan devices - wide bandgap is not all the same," *IET Circuits, Devices & Systems*, vol. 8, no. 3, pp. 227–236, 2014. DOI: https://doi.org/10.1049/iet-cds.2013.0223. [Online]. Available: https://ietresearch.onlinelibrary.wiley.com/doi/abs/10.1049/iet-cds.2013.0223.

[13] N. Iwamuro and T. Laska, "Igbt history, state-of-the-art, and future prospects," *IEEE Transactions on Electron Devices*, vol. 64, no. 3, pp. 741–752, 2017. DOI: 10.1109/TED.2017.2654599.

[14] "Mouser.nl." (), [Online]. Available: https://nl.mouser.com/.

[15] *Automotive n-channel 60 v (d-s) 175 °c mosfet*, Vishay, 2021. [Online]. Available: https://www.vishay.com/docs/76726/sqja16ep.pdf.

[16] *Eicedriver™ 2edi product family*, Infineon, 2021. [Online]. Available: https://nl.mouser.com/datasheet/2/196/Infineon_2EDS8265H_DataSheet_v02_07_EN-2943688.pdf.

[17] D. Such. "An arduino nano electronic speed controller (esc) — part 3." (2022), [Online]. Available: https://reefwing.medium.com/an-arduino-nano-electronic-speed-controller-esc-part-3-e17392bd2887.

[18] P. Wilson, "Chapter 4 - active components," in *The Circuit Designer's Companion (Fourth Edition)*, P. Wilson, Ed., Fourth Edition, Newnes, 2017, pp. 159–208, ISBN: 978-0-08-101764-7. DOI: https://doi.org/10.1016/B978-0-08-101764-7.00004-9. [Online]. Available: https://www.sciencedirect.com/science/article/pii/B9780081017647000049.

[19] *Rb160mm-60, schottky barrier diode*, ROHM Co., 2022. [Online]. Available: https://fscdn.rohm.com/en/products/databook/datasheet/discrete/diode/schottky_barrier/rb160mm-60tr-e.pdf.

[20] I. Rectifiers, *Hv floating mos-gate driver ics*, Application Note AN-978, Mar. 2007. [Online]. Available: https://www.infineon.com/dgdl/Infineon-HV_Floating_MOS_Gate_Drivers-ApplicationNotes-v01_00-EN.pdf?fileId=5546d4626c1f3dc3016c47de609d140a.

[21] jms. "Severe ringing effect when high side mosfet in half bridge switches on." (2014), [Online]. Available: https://electronics.stackexchange.com/questions/117360/severe-ringing-when-high-side-mosfet-in-half-bridge-circuit-switches-on.

[22] F. Semiconductors, *Suppressing mosfet gate ringing in converters: Selection of a gate resistor*, Application Bulletin AB-9, 1998. [Online]. Available: https://static5.arrow.com/pdfs/2004/0424/semi_ap/cs/fsc/application%5C%20note/ab-9.pdf.

[23] T. Instruments, *Bootstrap circuitry selection for half-bridge configurations*, Application Report SLUA887, Aug. 2018. [Online]. Available: https://www.ti.com/lit/an/slua887/slua887.pdf.

[24] *Coreless, high precision, hall-effect current sensor ic*, Allegro Microsystems, 2021. [Online]. Available: https://www.allegromicro.com/en/products/sense/current-sensor-ics/sip-package-zero-to-thousand-amp-sensor-ics/acs37612.

[25] J. Sylvestre. "Inverter dc link capacitor selection." (2019), [Online]. Available: https://www.specterengineering.com/blog/2019/9/7/dc-link-capacitor-selection-for-your-inverter.

[26] capacitor. "Aluminum electrolytic capacitor vs film capacitor." (2022), [Online]. Available: https://www.bm-cap.com/index.php/2022/09/13/aluminum-electrolytic-capacitor-vs-film-capacitor/#:~:text=Although%5C%20its%5C%20cost%5C%20is%5C%20slightly,continue%5C%20to%5C%20show%5C%20great%5C%20potential..

[27] *P78-500 non-isolated switching regulators*, CUI Inc., 2022. [Online]. Available: https://nl.mouser.com/datasheet/2/670/p78_500-3070515.pdf.

[28] *Wide input voltage range, 200ma uldo regulator*, Diodes incorporated, 2020. [Online]. Available: https://nl.mouser.com/datasheet/2/115/DIOD_S_A0011483360_1-2543654.pdf.

[29] B. Suppanz. "Pcb trace width calculator." (2018), [Online]. Available: https://www.4pcb.com/trace-width-calculator.html.

[30] J. Xu, J. Han, Y. Wang, S. Habib, and H. Tang, "A novel scalar pwm method to reduce leakage current in three-phase two-level transformerless grid-connected vsis," in *IEEE Transactions on Industrial Electronics*, vol. 67, 2020, pp. 3788–3797. DOI: 10.1109/TIE.2019.2920597.

[31] J. Paasschens, S. Harmsma, and R. Van der Toorn, "Dependence of thermal resistance on ambient and actual temperature," in *Bipolar/BiCMOS Circuits and Technology, 2004. Proceedings of the 2004 Meeting*, IEEE, 2004, pp. 96–99.

[32] M. Markovic, L. Saunders, and Y. Perriard, "Determination of the thermal convection coefficient for a small electric motor," in *Conference Record of the 2006 IEEE Industry Applications Conference Forty-First IAS Annual Meeting*, vol. 1, 2006, pp. 58–61. DOI: 10.1109/IAS.2006.256520.

[33] "Convective heat transfer," The Engineering ToolBox. (2003), [Online]. Available: https://www.engineeringtoolbox.com/convective-heat-transfer-d_430.html.

[34] M. Planck, *The Theory of Heat Radiation* (Dover Books on Physics Series). Dover Publications, 1991, ISBN: 9780486668116.

[35] W. Blevin and W. Brown, "A precise measurement of the stefan-boltzmann constant," *Metrologia*, vol. 7, no. 1, p. 15, 1971. DOI: 10.1088/0026-1394/7/1/003. [Online]. Available: https://dx.doi.org/10.1088/0026-1394/7/1/003.

[36] "Resistivity and conductivity temperature coefficients common materials," The Engineering ToolBox. (2003), [Online]. Available: https://www.engineeringtoolbox.com/resistivity-conductivity-d_418.html.

[37] S. Sakunthala, R. Kiranmayi, and P. Nagaraju Mandadi, "A study on industrial motor drives: Comparison and applications of pmsm and bldc motor drives," in *2017 International Conference on Energy, Communication, Data Analytics and Soft Computing (ICECDS)*, 2017, pp. 537–540. DOI: 10.1109/ICECDS.2017.8390224.

[38] L. Parsa and H. Toliyat, "Five-phase permanent-magnet motor drives," *IEEE Transactions on Industry Applications*, vol. 41, no. 1, pp. 30–37, 2005. DOI: 10.1109/TIA.2004.841021.

[39] P. Damodharan and K. Vasudevan, "Sensorless brushless dc motor drive based on the zero-crossing detection of back electromotive force (emf) from the line voltage difference," *IEEE Transactions on Energy Conversion*, vol. 25, no. 3, pp. 661–668, 2010. DOI: 10.1109/TEC.2010.2041781.

[40] S. Derammelaere, M. Haemers, J. De Viaene, F. Verbelen, and K. Stockman, "A quantitative comparison between bldc, pmsm, brushed dc and stepping motor technologies," in *2016 19th International Conference on Electrical Machines and Systems (ICEMS)*, 2016, pp. 1–5.

Appendices

Appendix A

Extra Equations

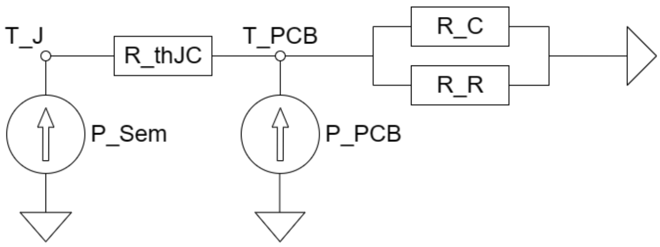

Figure A.1: Circuit modeling the power losses and dissipation of heat in the actual system. The power lost is represented as a current source and the dissipation of heat is represented by a resistance, with dissipation through radiation and convection modeled by R_R and R_C.

A.1 Dissipated power

Let's first consider the dissipated power [31]:

$$P_{diss} = \frac{T_J - T_a}{R_{thJA}} \tag{A.1}$$

This equation represents the power dissipated by the system. With T_J as the MOSFET junction temperature, T_a the ambient temperature selected as $25°$ C, R_{thJA} the thermal resistance of the MOSFET from junction to ambient air equal to $42°$ C/W, given by the data sheet [15].
The thermal resistance from junction to ambient R_{thJA} can be subdivided in three reactions of temperature exchange, from the junction of the transistor to the transistor case R_{thJC}, then followed by the two principles of convective and radiation heat transfer, represented in Figure 4.1 by R_C and R_R. To define those resistances the following formulas derived from [32] can be used,

$$R_C = \frac{1}{h_C A} \tag{A.2}$$

$$R_R = \frac{1}{h_R A} \tag{A.3}$$

With h_C as the convective heat transfer coefficient, h_R the radiation heat transfer coefficient, and A the surface which was taken to be 1inch^2 or (2.54 cm)^2 to stay consistent with R_{thJA} given in [15].
In turn, to calculate both coefficients, some formulas are available. The convective coefficient equation is determined empirically like in [33],

$$h_C = 12.12 - 1.16v + 11.6v^{\frac{1}{2}} \tag{A.4}$$

For wind speeds v directed towards the PCB, between 2 and 20 m/s.
And the radiation coefficient's formula was derived from [34],

$$h_R = \frac{\varepsilon\sigma(T_{PCB}^4 - T_a^4)}{T_{PCB} - T_a} \tag{A.5}$$

Where, ε represents the emissivity factor set as 0.8, σ the Stefan-Boltzmann constant equal to $5.67 \cdot 10^{-8}\ \frac{W}{\mathrm{m}^2 \cdot \mathrm{K}^4}$ [35]. T_{PCB} is the PCB temperature in K, and T_a the ambient temperature at $25\ ^\circ$ C.
A theoretical estimation of h_R can be done by taking the following assumptions, the equivalent resistance of the two parallel resistances R_C and R_R should be equal to $R_{thCA} = 41.7\ ^\circ$ C/W, representing the difference between the thermal resistance from junction to ambient $R_{thJA} = 42\ ^\circ$ C/W [15] and the thermal resistance from junction to case $R_{thJC} = 0.30\ ^\circ$ C/W [15], as seen in Figure 4.1. In analytical form,

$$R_{thCA} = \frac{1}{\frac{1}{R_C} + \frac{1}{R_R}} = \frac{1}{h_C A + h_R A} \tag{A.6}$$

It can then be rewritten to,

$$\frac{1}{R_{thCA} A} = h_R + h_C \tag{A.7}$$

By then choosing the value of h_C to be $12.12\ \frac{W}{m^2 ^\circ \mathrm{C}}$ when considering a wind speed of 0 m/s A.4, the theoretical value of h_R is found to be $25.0503\ \frac{W}{\mathrm{m}^2 ^\circ \mathrm{C}}$. The PCB temperature can then be calculated using the radiation coefficient h_R and the ambient temperature of 25 °C. The obtained PCB temperature reaches 413.705 °C.
Changing T_{PCB} to a more realistic value for example 120 °C and plugging it into equation A.5 to obtain a new value for h_R.

$$h_R = 0.8 * 5.67 * 10^{-8} \frac{393.15^4 - 298.15^4}{393.15 - 298.15} = 7.635 \frac{\mathrm{W}}{\mathrm{m}^2 ^\circ \mathrm{C}}$$

This new value for h_R can be then plugged back into equation A.7, defining the convection coefficient h_C to have the value of $29.535\ \frac{\mathrm{W}}{\mathrm{m}^2 ^\circ \mathrm{C}}$. The necessary wind speed to attain the value for h_C found above, can be identified by solving the system in equation A.4. The outcome of the formula gives a wind speed of ≈ 3.38 m/s.

Phase Current:

$$I_{ph} = \frac{P_{max}}{3E} = \frac{I_{dc} V_{dc}}{3 \frac{\omega}{k_v}} \tag{A.8}$$

DC current: $I_{dc} = 120$ A
DC voltage: $V_{dc} = 50.4$ V
Angular speed: $\omega = 0 \rightarrow 5000$ rpm
Voltage constant: $k_v = 240\ \frac{\mathrm{rpm}}{\mathrm{V}}$ [6]

Trace Resistance:

$$R_{trace} = R_{trace} + \alpha R_{trace}(T_J - T_a) \tag{A.9}$$

Measured resistance of the trace: $R_{trace} = 0.003\ \Omega$
Temperature coefficient of the resistance of copper: $\alpha = 4.29 * 10^{-3}\ \frac{1}{^\circ \mathrm{C}}$ [36]
Ambient temperature: $T_a = 25\ ^\circ$ C
Junction temperature: T_J [$^\circ$ C]

Average Current:

$$I_{av} = \frac{1}{\pi} \int_0^\pi I_{peak} sin(\theta) d\theta = \frac{2}{\pi} I_{peak} = \frac{2}{\pi} \sqrt{2} I_{ph} \tag{A.10}$$

Phase current: I_{ph} [A] see A.8

Appendix B

MATLAB Code

Temp_Model_4

```
%%%%%%%%%%%%%%%%%%%%%%%%%%%%%%%%%%%%%
% Author: Emeric de Galembert
% Date: 25/06/2023
% Function: Calculates the power losses of the circuit.
% Then uses a model to translate these in temperature rises
% of the different components at different rotational speeds of the motor.
%%%%%%%%%%%%%%%%%%%%%%%%%%%%%%%%%%%%%

% For the SQJA16EP transistor


k_v = 240; % voltage constant [rpm/V]
omega = 0:1:5000; %140000/28; % rotational speed[rpm]
E = omega/k_v; % induced voltage [V]
P_max = 6048; % max power through the system: 120A*50.4V [W]

I_ph = P_max./(3*E); % current per phase [A]
I_lim = 120; % current limit in the system
I_ph(I_ph > I_lim) = I_lim;

I_peak = sqrt(2)*I_ph; % peak current per phase [A]
I_av = 2/pi*I_peak; % average current over one switch [A] (defined through
 ↪ the integral of sin)
V_dc = 50.4; % supply voltage [V]
f_sw = 100000; % switching frequency [Hz]
t_on = 17*10^(-9); % typical turn on time [s]
t_off = 40*10^(-9); % typical turn off time [s]

T_a = 25; % ambient temperature [°C]
syms T_J; % junction temperature [°C]
R_thJA = 42; % thermal resistance of the MOSFET from junction to ambient
 ↪ [°C/W]
R_thJC = 0.30; % thermal resistance of the MOSFET from junction to case
 ↪ [°C/W]
R_thCA = 41.7/(11/6); % thermal resistance from case to ambient [°C/W]

temp = [25,125,175]; % temperature points needed to form a fit of the
 ↪ temperature behaviour of the MOSFET [°C]
resist = [0.003,0.00516,0.0065]; % on-state resistance at the points above
 ↪ [ohm]
```

```
test1 = polyfit(temp,resist,2); % fit of the temperature behaviour as a 2nd
 ↪  order polynomial
R_on = test1(1) * T_J.^2 + test1(2) * T_J + test1(3); % max on-resistance
 ↪  [ohm] (temp dependent)

alpha = 4.29*10^(-3); % temperature coefficient of resistance of copper
 ↪  [1/°C]
R_trace = 0.003+0.003*alpha*(T_J-T_a); % trace resistance [ohm]

P_MOSFET = 1/3*I_ph.^2.*R_on; % conduction losses [W]
P_SW = (V_dc*(t_on+t_off)*I_av.*f_sw)/(4*pi); % switching losses [W]
P_Sem = P_MOSFET+P_SW; % total losses in the transistor [W]
P_PCB = 1/6*I_ph.^2*R_trace; % losses in the traces around one transistor
 ↪  [W]
P_tot = P_Sem+P_PCB; % total power losses [W]

T_J0 = 120; % guess junction temperature [°C]


for i = 1:length(omega)
    P_Sem_filled(i) = double(subs(P_Sem(i),T_J,T_J0));
    P_PCB_filled(i) = double(subs(P_PCB(i),T_J,T_J0));
    P_tot_filled(i) = double(subs(P_tot(i),T_J,T_J0));
    T_Jnew(i) =
 ↪  T_a+(P_Sem_filled(i)*(R_thJC+R_thCA)+P_PCB_filled(i)*(R_thCA));
    T_PCB(i) = T_a+P_tot_filled(i)*(R_thCA);
    R_on_filled(i) = double(subs(R_on,T_J,T_Jnew(i)))
end


% figure;
% plot(omega, T_Jnew);
% xlabel('\omega (rpm)');
% ylabel('temperature (\circ C)');
% title('T_{J}');
%
% figure;
% plot(omega, T_PCB);
% xlabel('\omega (rpm)');
% ylabel('temperature (\circ C)');
% title('T_{PCB}');
%
% figure;
% plot(T_Jnew, R_on_filled);
% xlabel('temperature (\circ C)');
% ylabel('resistance (\Omega)');
% title('R_{on}');
%
% figure;
% plot(T_Jnew, P_Sem_filled);
% xlabel('temperature (\circ C)');
% ylabel('Power (W)');
% title('P_{Sem}');
%
% figure;
% plot(T_Jnew, P_PCB_filled);
% xlabel('temperature (\circ C)');
% ylabel('Power (W)');
```

```
% title('P_{PCB}');
%
% figure;
% plot(T_Jnew, P_tot_filled);
% xlabel('temperature (\circ C)');
% ylabel('Power (W)');
% title('P_{tot}');
```

Appendix C

Simulations

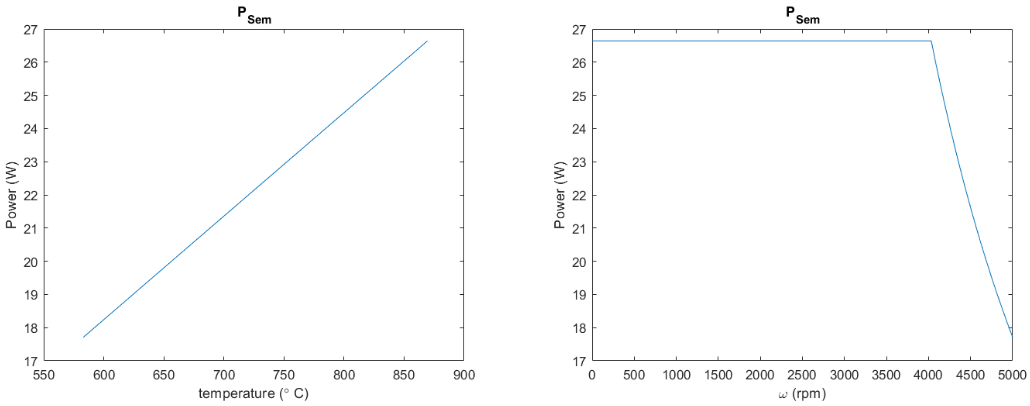

Figure C.1: Left: Graph of the relation between the junction temperature and the power losses in the semiconductor.
Right: Graph of the relation between the rotational speed and the power losses in the semiconductor.

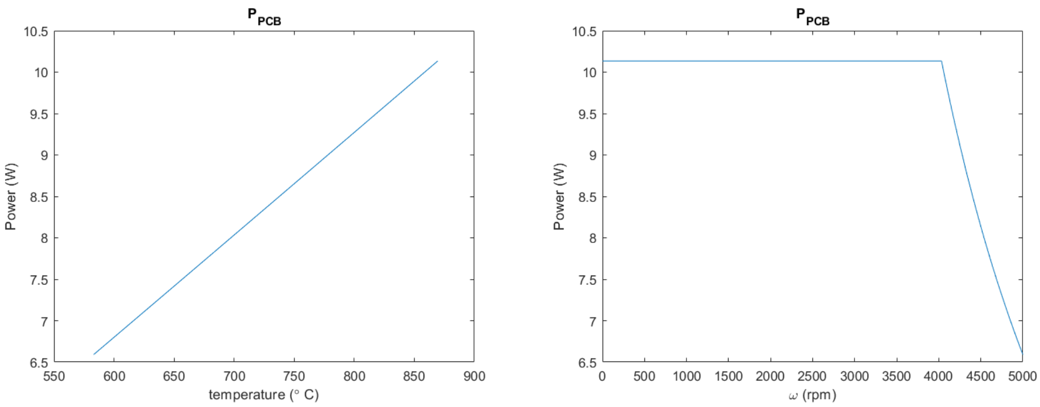

Figure C.2: Left: Graph of the relation between the junction temperature and the power losses in the PCB.
Right: Graph of the relation between the rotational speed and the power losses in the PCB.

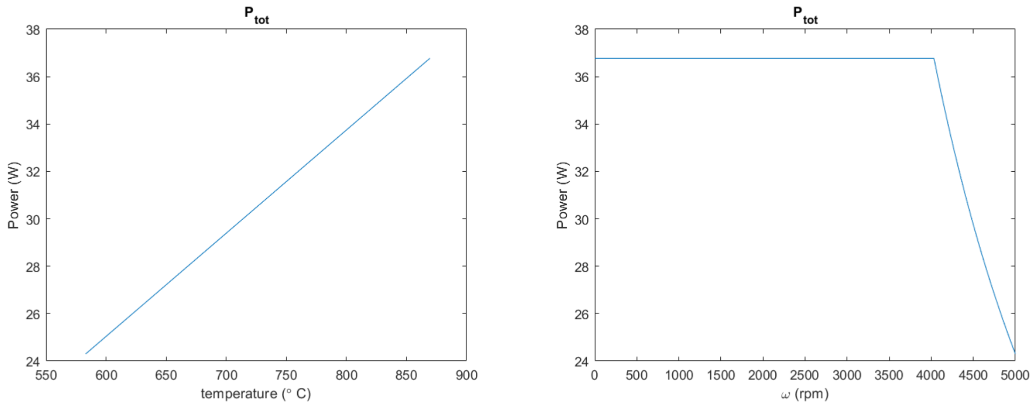

Figure C.3: Left: Graph of the relation between the junction temperature and the total power losses. Right: Graph of the relation between the rotational speed and the total power losses.

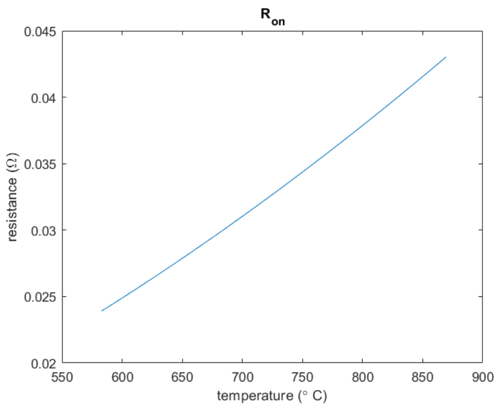

Figure C.4: Graph of the relation between the junction temperature and the on-resistance of the MOSFET.

Appendix D

Converter circuit schematic

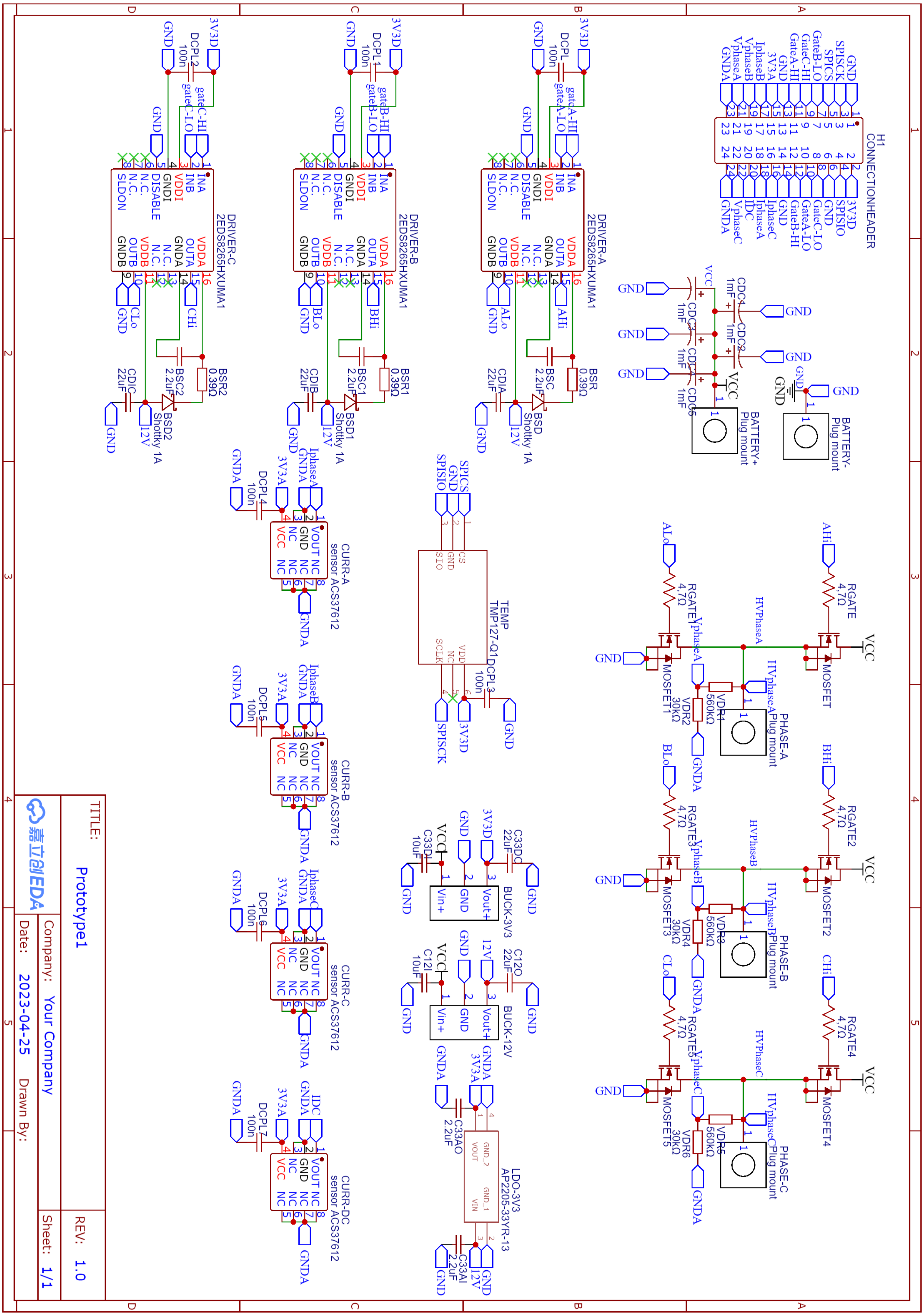

Figure D.1: Schematic of the complete inverter circuit. This is the second prototype that was realized by the team.

Appendix E

Converter PCB lay-out

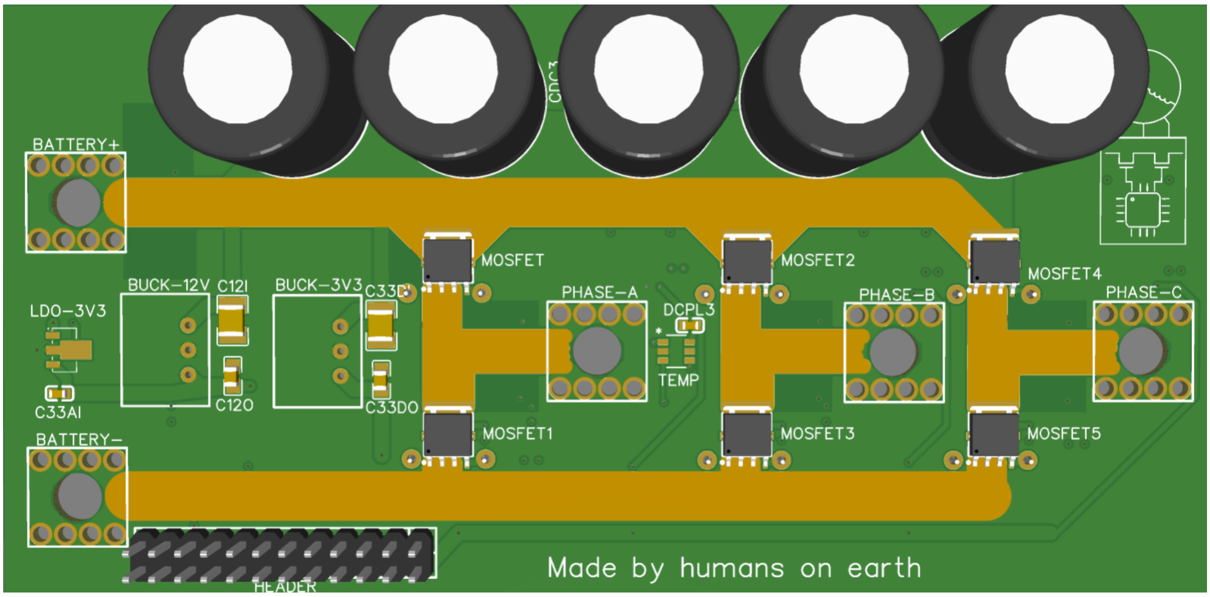

Figure E.1: Render of the second prototype PCB from the front.

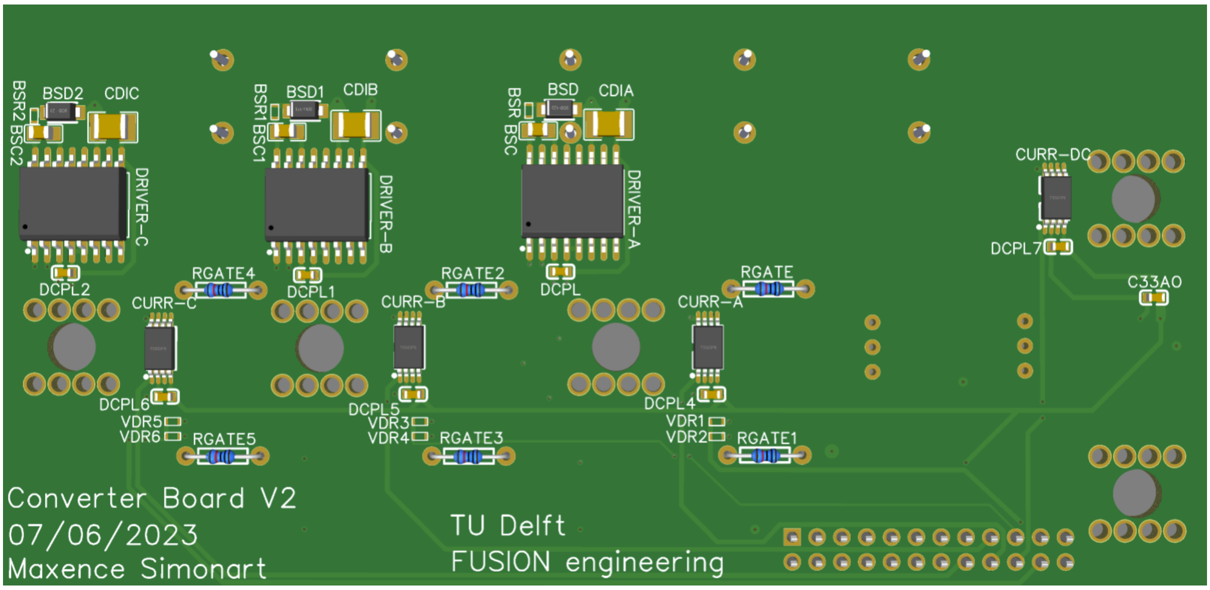

Figure E.2: Render of the second prototype PCB from the back.

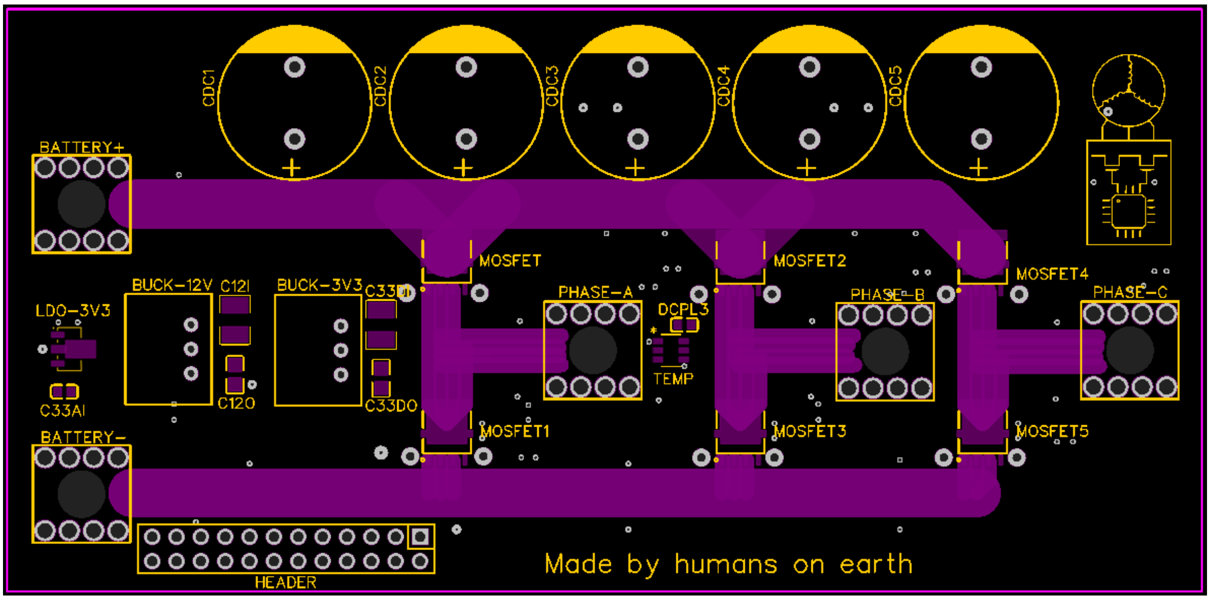

Figure E.3: Figure showing the exposed copper, of which the high current traces which are covered in melted solder.

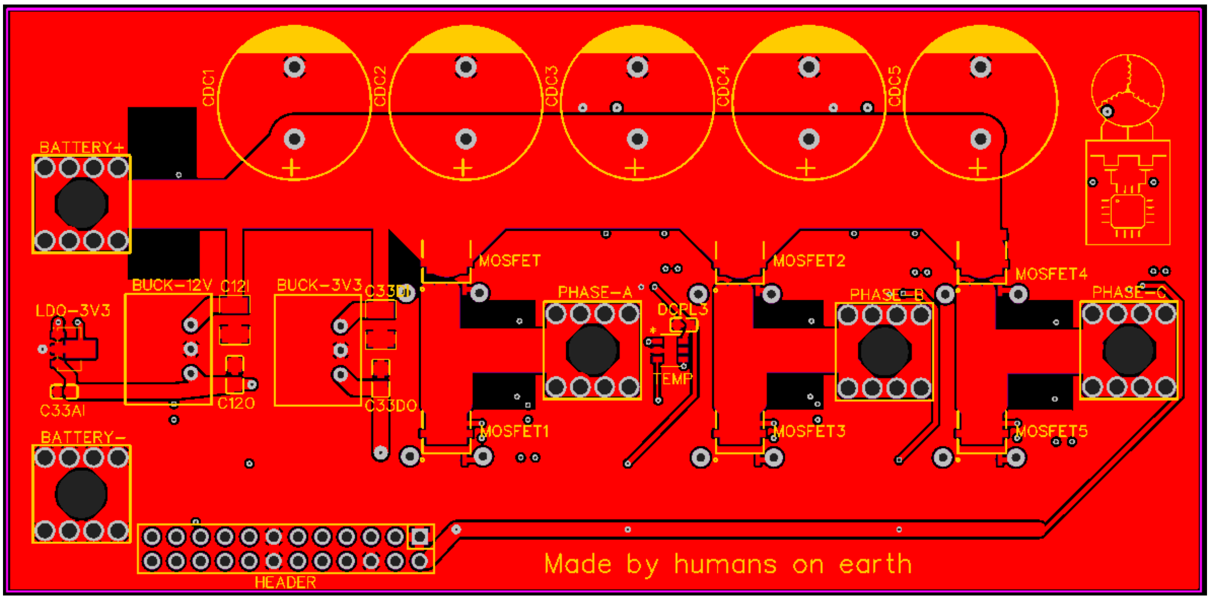

Figure E.4: Figure showing the routing on the top layer of the PCB

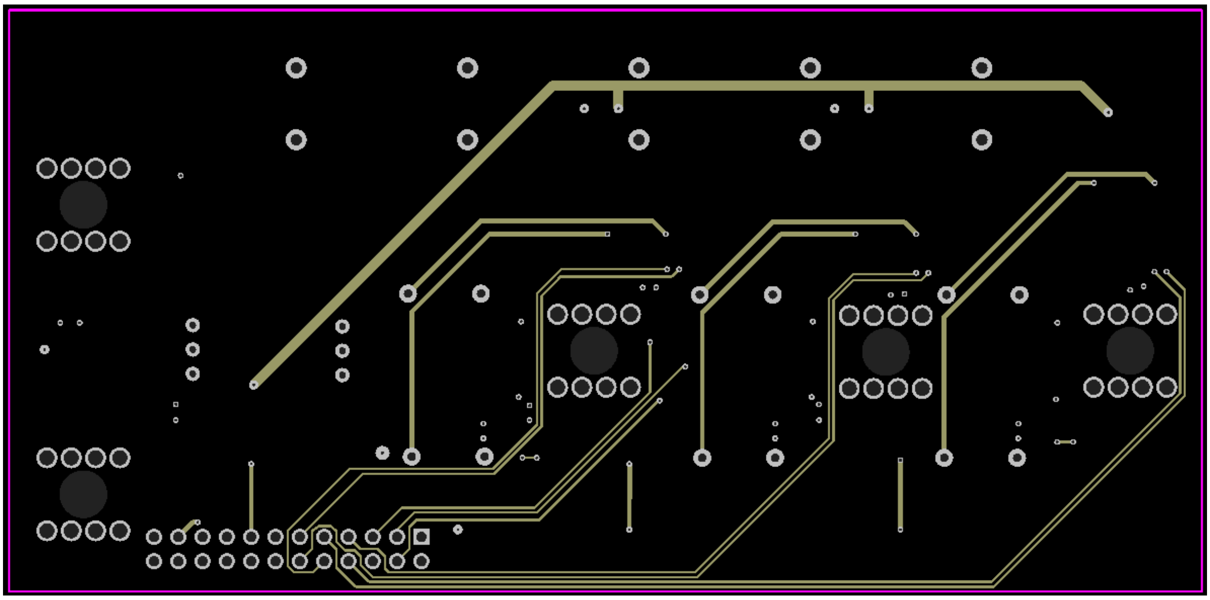

Figure E.5: Figure showing the routing of the digital lines on the second layer of the PCB.

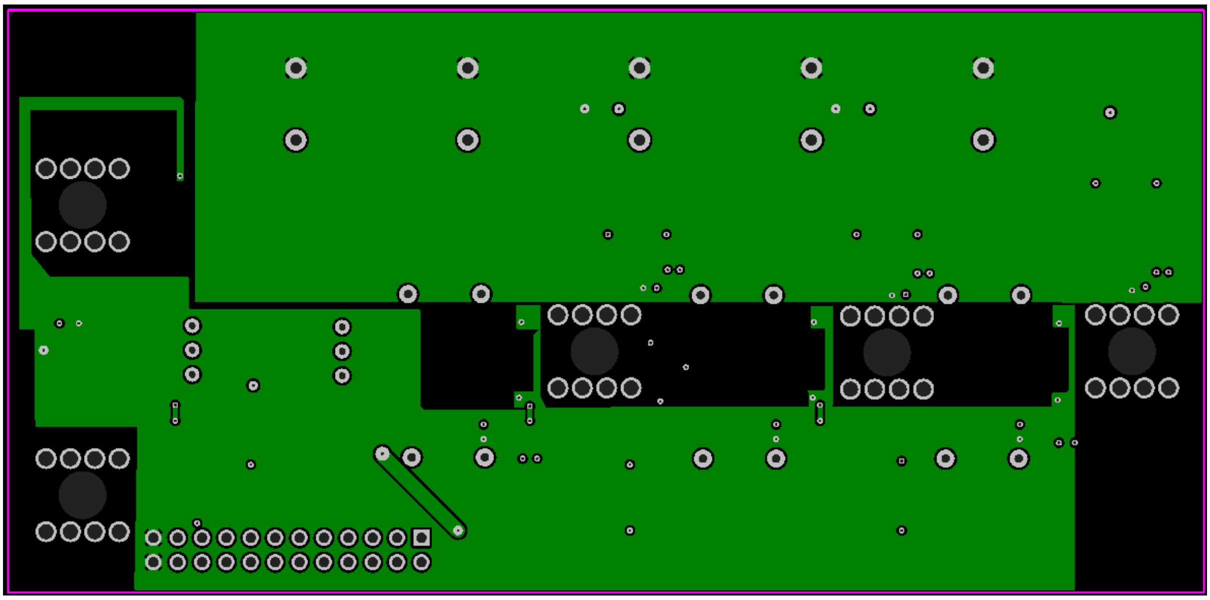

Figure E.6: Figure showing the digital ground (top) and the analog ground (bottom) on the third layer of the PCB.

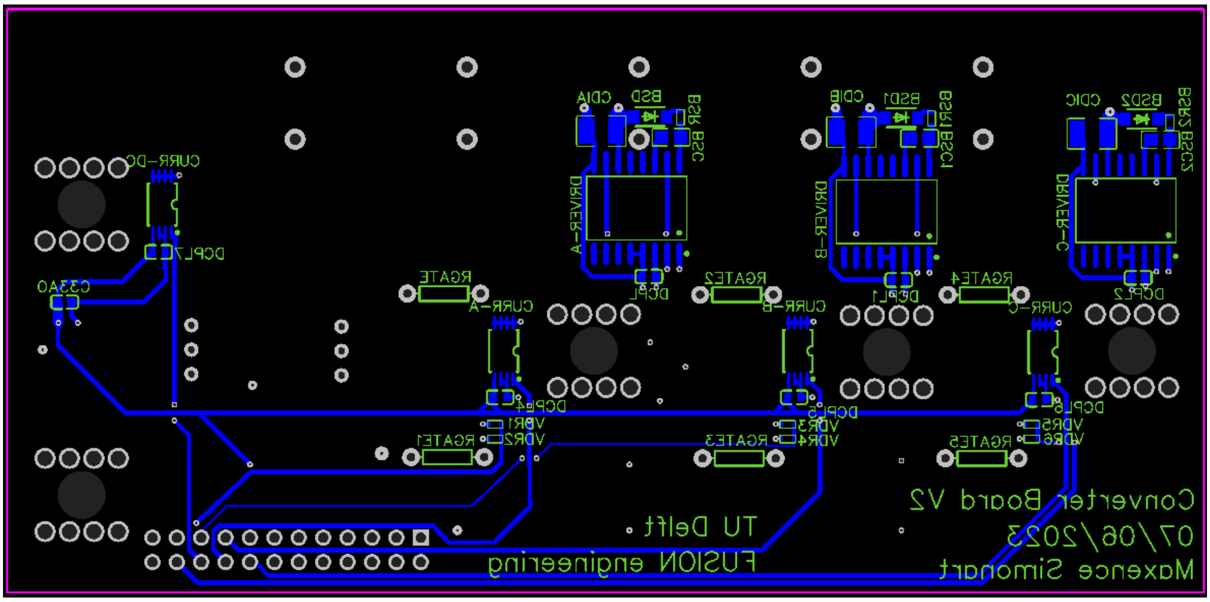

Figure E.7: Figure showing the routing of the analog sensor signal lines as well as the digital gate driver assemblies on the bottom layer of the PCB.

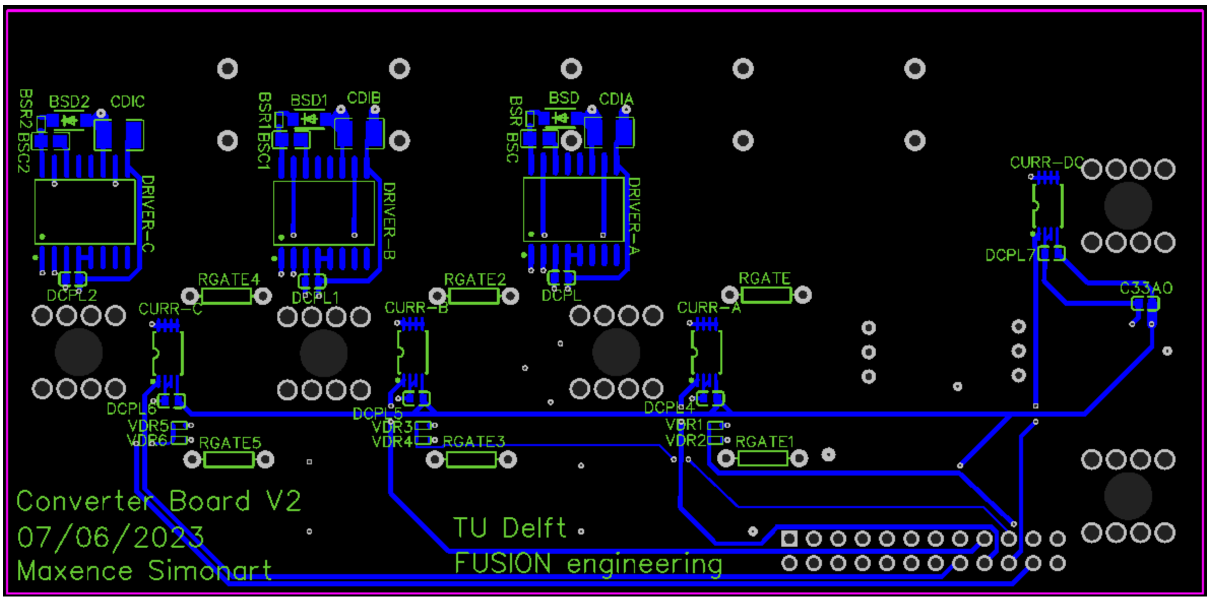

Figure E.8: Figure showing the mirrored bottom layer of the PCB for additional clarity.

Appendix F

Motor types

This section will be looking at the similarities and differences between BLDC (brushless direct current) and PMSM (permanent magnet synchronous motor) motors. Both a BLDC and PMSM motor are low-cost devices that require less maintenance than other motor types. Other advantages of these types of motors are their robustness, higher torque and speed bandwidths, their high efficiency, and their high power density. [37]
The BLDC motor is defined by its trapezoidal shaped induced electromotive force [38], [39]. The BLDC motor is popular in industry because of how simple it is to control. The control algorithm consists of six distinct steps that should be switched between at six discrete stator positions. [37], [40]
In contrast, a PMSM motor is defined by its sinusoidal induced electromotive force [38]. This type of motor is more challenging to drive as it ideally requires three sinusoidal sources to be applied with a 120 degree phase difference between them. To determine the instantaneous current that should be applied to the motor, an accurate rotation of the stator should be available at all times. [37], [40]
The differences discussed above result in differences in various aspects of these motors, these are discussed in F.1.

Table F.1: A table of differences between BLDC and PMSM motors, from [37] with modifications from [38], [40]

BLDC	**PMSM**
fed with rectangular current waveforms	fed with sinusoidal currents
trapezoidal back emf	sinusoidal back emf
discrete stator sensing, every 60 degrees	continuous stator sensing
two phases are powered at the same time	three phases are powered at the same time
torque ripple	no torque ripple
high core losses due to harmonic content	less core loss
less switching losses	high switching loss at same frequency
simpler control algorithm	more complex control algorithm
does not work on distributed winding	does work on distributed winding
not as efficient, lower torque	more efficient, higher torque